Joule

CellPress

Article

Solvent-Dependent Oxidizing Power of LiI Redox Couples for Li-O_2 Batteries

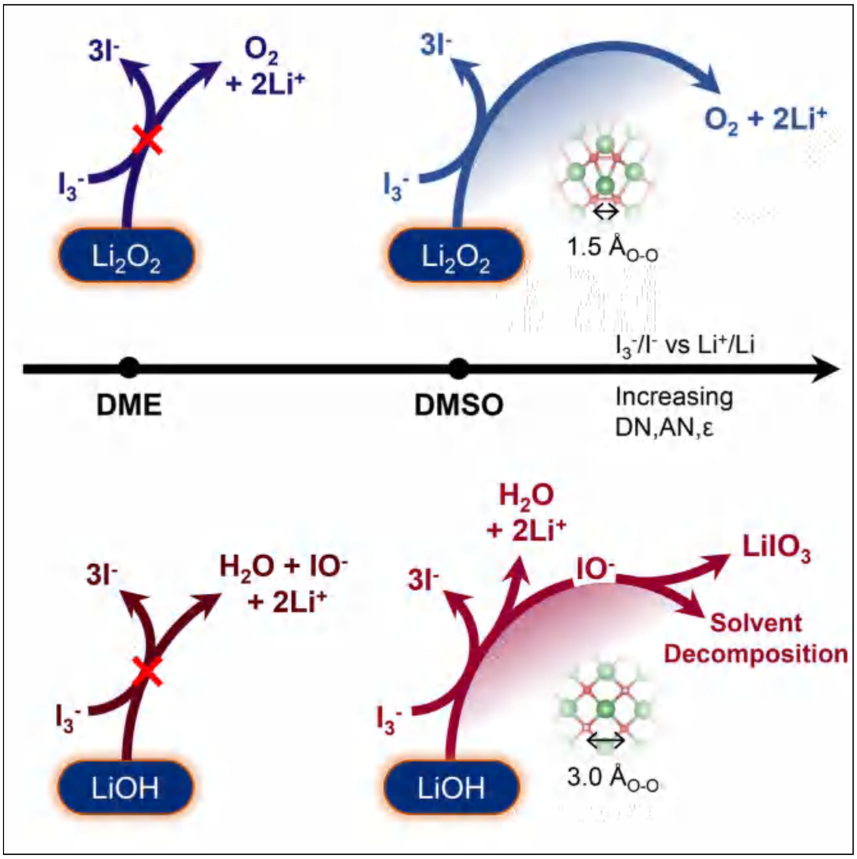

Stronger solvation of I^- and Li^+ ions enables the oxidation of Li_2O_2 to O_2 and LiOH to $LiIO_3$ by I_3^- in DMSO, whereas no reaction occurs in DME as a result of the insufficient thermodynamic driving force. Solvation effects can dramatically influence the performance of soluble redox mediators for Li-O_2 batteries by altering thermodynamics and reactivity of the mediators.

Graham Leverick, Michał Tułodziecki, Ryoichi Tatara, Fanny Bardé, Yang Shao-Horn

leverick@mit.edu (G.L.)
shaohorn@mit.edu (Y.S.-H.)

HIGHLIGHTS

Solvation energy of I^- and Li^+ dictate the reactivity between I_3^- and Li_2O_2/LiOH

I_3^- and I_2 react irreversibly with LiOH to form $LiIO_3$ at potentials above ~3.1 V_{Li}

Electrolytes can critically alter the performance of Li-O_2 soluble redox mediators

Leverick et al., Joule 3, 1106–1126
April 17, 2019 © 2018 Elsevier Inc.
https://doi.org/10.1016/j.joule.2018.12.014

Joule

CellPress

Article

Solvent-Dependent Oxidizing Power of LiI Redox Couples for Li-O_2 Batteries

Graham Leverick,[1,5,*] Michał Tułodziecki,[2] Ryoichi Tatara,[2] Fanny Bardé,[3] and Yang Shao-Horn[1,4,*]

Context & Scale

Rechargeable, nonaqueous lithium-oxygen (Li-O_2) batteries offer high theoretical gravimetric energy but suffer from considerable fundamental issues relating to cycle life, parasitic reactions, and poor round-trip efficiency, in part, because of poor kinetics during charge. Soluble redox mediators, such as LiI, have been proposed as a solution to this problem, but despite promising initial results, there exists considerable discrepancy in literature regarding the oxidizing power of I_3^-/I_2 (oxidized species formed during charge) against Li_2O_2 and LiOH (possible discharge products of the Li-O_2 chemistry). In this study, we use detailed quantifications, a wide range of characterization techniques, and cells constructed with a solid Li-conducting separator to eliminate shuttling to resolve these ambiguities. We show that the oxidizing power of I_3^- is solvent dependent and that Li_2O_2 is oxidized to O_2, whereas LiOH irreversibly forms IO^-, which can either form $LiIO_3$ or attack solvent molecules.

SUMMARY

Li-O_2 batteries offer higher gravimetric energy density than commercial Li-ion batteries. Despite this promise, catalyzing oxidation of discharge products, Li_2O_2 and LiOH, during charging remains an obstacle to improved cycle life and round-trip efficiency. In this work, reactions between LiI, a soluble redox mediator added to catalyze the charging process, and Li_2O_2 and LiOH are systematically investigated. We show that stronger solvation of Li^+ and I^- ions led to an increase in the oxidizing power of I_3^-, which allowed I_3^- to oxidize Li_2O_2 and LiOH in DMA, DMSO, and Me-Im, whereas in weaker solvents (G4, DME), the more oxidizing I_2 was needed before a reaction could occur. We observed that Li_2O_2 was oxidized to O_2, whereas LiOH reacts to form IO^-, which could either disproportionate to $LiIO_3$ or attack solvent molecules. This work clarifies significant misconceptions in these reactions and provides a thermodynamic and selectivity framework for understanding the role of LiI in Li-O_2 batteries.

INTRODUCTION

There has been considerable interest in nonaqueous Li-O_2 batteries in the past decade because of their high theoretical gravimetric energy density (potentially up to three times that of commercial lithium-ion [Li-ion] batteries).[1–3] This large theoretical improvement in gravimetric energy density stems from the fundamentally different reactions of the Li-O_2 battery chemistry, which rely on reducing gaseous oxygen to form solid lithium peroxide ($2Li + O_2 = Li_2O_2$, $E^0 = 2.96\ V_{Li}$) or lithium oxide ($4Li + O_2 = 2Li_2O$, $E^0 = 2.91\ V_{Li}$).[4] Previous work shows that the discharge of nonaqueous Li-O_2 batteries can produce Li_2O_2 with low overpotential,[5] the morphology of which is dependent on the solvent,[6,7] counter anion,[8,9] and potential or rate.[10,11] Unfortunately, charging Li-O_2 batteries with nonaqueous electrolytes requires a high overpotential to liberate molecular oxygen and this reaction is considerably more irreversible at high potentials, as shown by McCloskey et al.,[12] leading to poor round-trip efficiency and cycle life resulting from parasitic side reactions.[1,3] Therefore, considerable efforts have been placed on attempting to catalyze the charging process in Li-O_2 batteries.[13–37]

While solid-state catalysts have been employed to reduce the overpotential during charge, including metal oxides,[31,32] modified carbon,[33–35] and metals or metal alloys,[35,38] these catalysts rely on good electrical contact between Li_2O_2 and the catalyst throughout the entire charging process,[37] cannot oxidize Li_2O_2 that forms electronically isolated from the positive electrode,[39] and do not suppress side reactions during charging.[36] An alternative approach is the use of soluble redox mediators to promote electron transfer to the surface of the electronically insulating Li_2O_2,[40] where the redox mediator is first electrochemically oxidized at the electrode surface and then the oxidized form of the redox mediator chemically oxidizes Li_2O_2 to form Li^+ ions and molecular oxygen and regenerate the reduced form of the redox mediator. Many organic molecules such as TEMPO,[16,41–43] TDPA,[22] and TTF[23] as well as inorganics such as LiI[14,15,18] and LiBr[17] have been proposed as redox mediators. Lithium iodide (LiI) has received considerable attention owing to a number of studies suggesting high cycling performance.[14,15] Lim et al.[14] have suggested stable cycling with low overpotential over 900 cycles using LiI as a soluble redox mediator in a tetraglyme (G4) electrolyte with a CNT fibril electrode. In addition, Liu et al.[15] have claimed to achieve 2,000 cycles using LiI in a 1,2-dimethoxyethane (DME)-based electrolyte containing ~5v% H_2O with a reduced graphene oxide electrode and lithium hydroxide (LiOH) as the dominant discharge product. However, ambiguities exist regarding the influence of LiI on both the discharge[44–46] and charge[18,44,46,47] processes.

Recent studies have clarified the role of LiI addition in the electrolyte on discharge, the addition of which can change the dominant discharge product from Li_2O_2 to LiOH,[15,18,44–46] $LiOH \cdot H_2O$,[45] or $LiOOH \cdot H_2O$[45,48] by decreasing the pK_a of water in the electrolyte.[45] Adding water to DME-based electrolytes up to 5,000 ppm[49] results in Li_2O_2 on discharge when no LiI is present. On the other hand, the dominant discharge product can become LiOH ($H_2O > \sim 500$ ppm)[44,45] or LiOOH ($H_2O > \sim 5$v%)[45,48] when both LiI and water are present. The formation of LiOH and related products can be attributed to the lowered deprotonation energy of water, which occurs with stronger solvation of water molecules by organic solvent molecules such as acetonitrile (MeCN) (Kwabi et al.[49]) and/or the interactions between water molecules and strongly interacting anions such as I^-.[45] While some studies[18,46] have proposed the proton source for LiOH is the iodide-catalyzed decomposition of glyme-based solvents (such as DME and G4), both Burke et al.[44] and Tułodziecki et al.[45] have demonstrated stable coexistence of iodide and DME accompanied by Li_2O_2 formation on discharge under rigorously anhydrous conditions, and computational studies[50] indicate that water is the energetically preferred proton source.

Unfortunately, ambiguities still exist regarding what oxidized iodide species (I_3^- and I_2) can decompose Li_2O_2 and LiOH and whether molecular oxygen is formed upon charging in the presence of LiI. Qiao et al.[46] have reported that I_3^- can oxidize peroxide-like species to form O_2 with water addition (up to 30v%) in G4, whereas other studies have shown that I_2, which is more oxidizing than I_3^-, is required to oxidize Li_2O_2 and generate molecular O_2 in anhydrous DME[44] and G4.[18,47,48] Similarly, Zhu et al.[48] argue for the oxidation of $LiOOH\text{-}H_2O$ in diglyme (G2) and DMSO with 9.1v% water by I_3^- to form O_2 as well as the oxidation of LiOH by I_2 to form O_2. Liu et al.[15] suggested that I_3^- can oxidize LiOH formed in DME and G4 (with the addition of ~5v% water) to generate O_2. In contrast, the concept of LiOH oxidation to O_2 by I_3^- is rebutted by a few studies[44,46,51] including Viswanathan et al.[52] arguing that the oxidation of LiOH by I_3^- is thermodynamically uphill in DME. This argument is in agreement with findings from Qiao et al.[46] who report that LiOH cannot be oxidized in the presence of I_3^- and I_2, and Burke et al.[44] who show that LiOH irreversibly forms lithium iodate ($LiIO_3$) from I_2 in DME instead of evolving O_2. Although some of the reported discrepancies may come from a lack of rigorous quantification of reaction products to ensure the amount of oxygen detected is the dominant path of the reaction[48] or a misidentification of $LiOOH\text{-}H_2O$ formed on discharge[15] because of its subsequent disproportionation to LiOH,[45] the discrepancies found for the oxidation of Li_2O_2 and LiOH by I_3^- and I_2 in previous work may primarily result from the solvent-dependent oxidizing power of I_3^- and I_2 against Li_2O_2 and LiOH. I^- ions can go through two distinct redox transitions during oxidation in aprotic electrolytes, having first iodide anions (I^-) oxidized to form triiodide (I_3^-) and I_3^- oxidized

[1] Department of Mechanical Engineering, Massachusetts Institute of Technology, 77 Massachusetts Avenue, Cambridge, MA 02139, USA

[2] Research Laboratory of Electronics, Massachusetts Institute of Technology, 77 Massachusetts Avenue, Cambridge, MA 02139, USA

[3] Research & Development 3, Advanced Technology 1, Toyota Motor Europe, Hoge Wei 33 B, Zaventem 1930, Belgium

[4] Department of Materials Science and Engineering, Massachusetts Institute of Technology, 77 Massachusetts Avenue, Cambridge, MA 02139, USA

[5] Lead Contact

*Correspondence: leverick@mit.edu (G.L.), shaohorn@mit.edu (Y.S.-H.)

https://doi.org/10.1016/j.joule.2018.12.014

to form iodine (I_2),[53] where the potentials of the I^-/I_3^- and I_3^-/I_2 redox transitions can be significantly influenced by solvent.[52–54] While it has been previously suggested that changes in these redox potentials may be important for the performance of LiI as a redox mediator in Li-O_2 batteries,[26,52] this effect has not been studied systematically.

In this paper, we examine the role of LiI on the charging process of Li-O_2 batteries by systematically studying the solvent-dependent oxidizing power of I_3^-/I^- and I_2/I_3^- toward Li_2O_2 and anhydrous LiOH. The oxidizing power of I_3^-/I^- and I_2/I_3^- toward Li_2O_2 and LiOH was studied chemically by quantifying the consumption of I_3^- upon addition of Li_2O_2 synthesized from disproportionation, where the liquid reaction products were examined using UV-vis spectroscopy and ^1H NMR, the solid reaction products were studied by Raman spectroscopy and XRD, and the gaseous products were assessed using gas chromatography and mass spectrometry. In addition, the role of I^- on the charging of Li-O_2 batteries and LiOH-pre-loaded cells was examined using differential electrochemical mass spectroscopy (DEMS), where the amount of oxygen release was quantified. We show that I_3^-/I^- potentials increase with greater solvent Gutmann acceptor number (AN) and dielectric constant, suggesting stronger solvation of I^- while I_2/I_3^- redox potentials are largely solvent independent. Therefore, stronger solvation of Li^+ (as previously reported by Kwabi et al.[6]) and I^- ions in solvents such as DMA, DMSO, and Me-Im can increase the oxidizing power of I_3^-/I^-, allowing I_3^- to effectively oxidize Li_2O_2 to generate O_2, which was supported by chemical and electrochemical measurements. On the other hand, in solvents where both I^- and Li^+ are weakly solvated such as glymes, I_3^-/I^- redox potentials are not high enough to oxidize Li_2O_2, and more oxidizing I_2 is required for the oxidation of Li_2O_2 to O_2 to proceed. The reactions between anhydrous LiOH and I_3^- were also found to be solvent dependent, where no reaction was observed in G4, DME, and pyridine while the reaction proceeded to completion in DMA, DMSO, and Me-Im where the I_3^-/I^- redox potential was above ~3.1 V_{Li}. We show that the reaction between anhydrous LiOH and oxidized iodide species produced water and a hypoiodite (IO^-) intermediate, which could either disproportionate to form $LiIO_3$ or attack solvent molecules and result in decomposition products such as dimethyl sulfone ($DMSO_2$). From GC and MS of *ex situ* reactions and DEMS during the charging of pre-loaded LiOH electrodes, no O_2 gas evolution was observed during the reaction between LiOH and oxidized iodide species. We propose that the selectivity between O_2 and the thermodynamically preferred $LiIO_3$ is governed by a kinetic barrier relating to O-O bond dissociation and this kinetic barrier prevents IO^- formation, allowing for the evolution of gaseous O_2 when oxidizing Li_2O_2, which was supported by reactions between oxidized iodide species and KO_2 and Li_2O.

RESULTS

Solvent-Dependent Potentials of I_3^-/I^-

The redox potential of I_3^-/I^- was shown to shift positively against the reference redox potential of decamethylferrocene ($Me_{10}Fc$) from DME, to DMA, to DMSO, while that of I_3^-/I_2 remained nearly constant (Figures 1 and S1). The use of the solvent-insensitive redox potential of $Me_{10}Fc$[55,56] as a reference is preferred to the solvent-dependent Li^+/Li potential[57] and allows for a meaningful determination of solvation energy influence on the solvent-dependent redox potentials of I_3^-/I^- and I_3^-/I_2. The reduction and oxidation peaks of the I_3^-/I^- (centered between 0.02 and 0.23 V_{Me10Fc}) and I_3^-/I_2 (centered at ~0.64 V_{Me10Fc}) couples were observed in cyclic voltammograms (CVs), from which the redox potentials of I_3^-/I^- and I_3^-/I_2

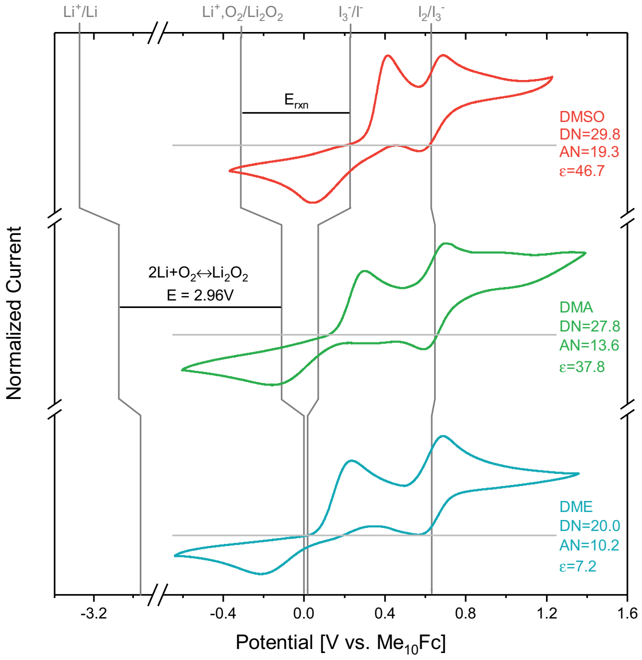

Figure 1. Solvent-Dependent Redox Potentials of I_3^-/I^-

Cyclic voltammograms of solutions of 0.5 M LiTFSI + 10 mM LiI collected at 100 mVps under argon environment in each of the considered solvents with a Pt working electrode, either Li metal (DME, DMSO) or lithium titanium oxide (DMA) counter electrode, and Ag/Ag$^+$ reference electrode. Currents were normalized based on the maximum current observed. Li$^+$/Li potentials were measured in each solvent using a piece of Li metal, and the Li$^+$,O$_2$/Li$_2$O$_2$ potential was fixed at 2.96 V$_{Li}$.

were obtained by averaging the reduction and oxidation peak centers (Figures 1 and S1; Table S1). These measurements were collected using a Pt macroelectrode as the working electrode and Ag$^+$/Ag as the reference electrode in solvents containing 10 mM LiI with 0.5 M LiTFSI under an argon environment, where the Ag$^+$/Ag reference electrode potential scale was converted to that of Me$_{10}$Fc following previous work[6] (Figure S2) for each solvent. The shifts in the potential of the I_3^-/I^- redox were plotted against the reported Guttmann acceptor number (AN), Guttmann donor number (DN), and dielectric constant (ε) for these solvents (Figures S3–S5). We propose that the positive shift in the potential of I_3^-/I^- can be attributed to increasing thermodynamic stability of the I^- ion through solvation via higher AN, higher dielectric constant,[53] and possibly through the formation of ion pairs with Li$^+$.[48] We anticipate that the solvation influences I^- ions more than I_3^- in this redox couple as there are three I^- ions for each I_3^- and the larger I_3^- ions (which are more charge diffuse) might interact with the solvent less. Following the same argument, the solvent-insensitive redox potential of I_2/I_3^- can be attributed to the weak solvation of I_3^- and I_2 in the considered solvents.

This positive shift in the potential of I_3^-/I^- increases its oxidizing power toward Li_2O_2 (or the thermodynamic driving force to oxidize Li_2O_2) to evolve O_2 ($Li_2O_2 \rightarrow 2Li^+ + O_2 + 2e^-$), with a trend of DME < DMA < DMSO. Considering that the Li$^+$/Li potential decreases from DME, to DMA, to DMSO on the Me$_{10}$Fc scale (Figure 1) as a result of stronger lithium solvation with higher DN[6,7] and higher dielectric constant (the Born model)[58,59] and that the free energy of O_2 and Li_2O_2 are solvent independent, the redox potential of Li$^+$,O$_2$/Li$_2$O$_2$ would follow the same trend as the Li$^+$/Li potential,[6] decreasing from 0.00 V$_{Me10Fc}$ in DME, to −0.11 V$_{Me10Fc}$ in DMA, and −0.31 V$_{Me10Fc}$

in DMSO. Therefore, as the potential of I_3^-/I^- shifts to higher values from DME, to DMA, to DMSO and that of $Li^+,O_2/Li_2O_2$ moves to lower values on the $Me_{10}Fc$ scale, the oxidative power of I_3^-/I^- toward Li_2O_2 increases, from 0.04 eV in DME, to 0.36 eV in DMA and 1.08 eV in DMSO (where positive values indicate a spontaneous reaction between I_3^- and Li_2O_2). Using the linear free energy relationship that links thermodynamics and kinetics,[60] one would anticipate that the kinetics of Li_2O_2 oxidation by I_3^- would significantly increase from DME, DMA, to DMSO. Solvents with higher AN and DN, such as DMSO, which is responsible for increased oxidative power of I_3^-/I^- toward Li_2O_2 through stronger solvation of Li^+ and I^-, tend to have higher viscosity (Table S2); however, higher AN and DN solvents also lead to increased salt dissociation, as evidenced by a higher Walden product (Table S2), leading to comparable ionic conductivities of a 0.5M LiTFSI solution in DME (6.96 mS/cm), DMA (9.05 mS/cm), and DMSO (6.59 mS/cm).

Solvent-Dependent Oxidizing Power of I_3^-/I^- and I_2/I_3^- toward Li_2O_2

The solvent-dependent oxidizing power of I_3^-/I^- toward Li_2O_2 was examined by adding 1 mL of 50 mM I_3^- (50 mM I_2 + 0.2 M LiI, $I^-:I_2 = 4:1$) in different solvents to Li_2O_2 (100 μmol, $Li_2O_2:I_3^- = 2:1$). Li_2O_2 was first synthesized through disproportionation by adding 1 mL of 0.4M LiTFSI to KO_2 (200 μmol, LiTFSI:KO_2 = 2:1). The initially brown-colored solution obtained after mixing 50 mM I_3^- with the synthetic Li_2O_2 became clear in DMA (<24 h), DMSO (~1 min), and Me-Im (~10 s), as shown in Figure 2A. On the other hand, the brown color became less pronounced for pyridine, whereas no visible color change was found for DME and G4 after 24 h. The color change observed for DMA, DMSO, and Me-Im can be attributed to the reduction of I_3^- (dark brown) to I^- (colorless). This hypothesis is supported by UV-vis spectroscopy of the liquid phase decanted from the reaction mixture after 24 h, where characteristic peaks for I_3^- at 293 nm and 364 nm disappeared for DMA, DMSO, and Me-Im, whereas those for DME, G4, and pyridine remained, as shown in Figures 2B, S6, and S7. The consumption of I_3^- after 24 h was quantified using the absorbance of I_3^- solutions with known concentrations (as detailed in Figures S8–S11) and was found to increase with greater redox potentials of I_3^-/I^- from G4, DME, pyridine, to DMA (DMSO or Me-Im) on the $Me_{10}Fc$ scale (Figures 1 and S1), where these higher redox potentials relative to $Li^+,O_2/Li_2O_2$ resulted in a larger thermodynamic driving force to oxidize Li_2O_2, as shown in Figure 2C. Larger thermodynamic driving forces for the oxidation of Li_2O_2 by I_3^- in DMA, DMSO, and Me-Im were found to correlate well with higher reaction rate constants calculated based on an assumed first-order dependence on the concentration of I_3^- (Figure S12), which supports the anticipated linear free energy relationship that links thermodynamics and kinetics.[60] Raman spectra of the solid recovered after the reaction between Li_2O_2 and I_3^- revealed Li_2O_2 remained after the reaction as Li_2O_2 was two times overstoichiometric (Figure S13). Further support for Li_2O_2 oxidation by I_3^- in DMSO came from oxygen evolution as detected by gas chromatography (Figure S14) and mass spectroscopy (Figure 3), which accompanied color changes of the solution during the reaction given by $I_3^- + Li_2O_2 \rightarrow 2Li^+ + 3I^- + O_2$. Therefore, having solvents not only with higher AN to increase the potential of I_3^-/I^- but also with higher DN to lower the potential of $Li,O_2/Li_2O_2$, such is the case in DMA, DMSO, and Me-Im, promotes the oxidizing power of I_3^-/I^- toward Li_2O_2 as opposed to solvents such as G4 and DME. The solvent-dependent oxidizing power of I_3^- against Li_2O_2 is supported by a recent study, where Nakanishi et al.[57] have shown that the thermodynamic shifts in the iodide redox on a lithium scale resulting from the effect of solvent and lithium concentration can change the oxidizing power of I_3^- against Li_2O_2 in 1 M and 2.8 M LiTFSI electrolytes in DMSO and G4 with 0.1 M LiI.

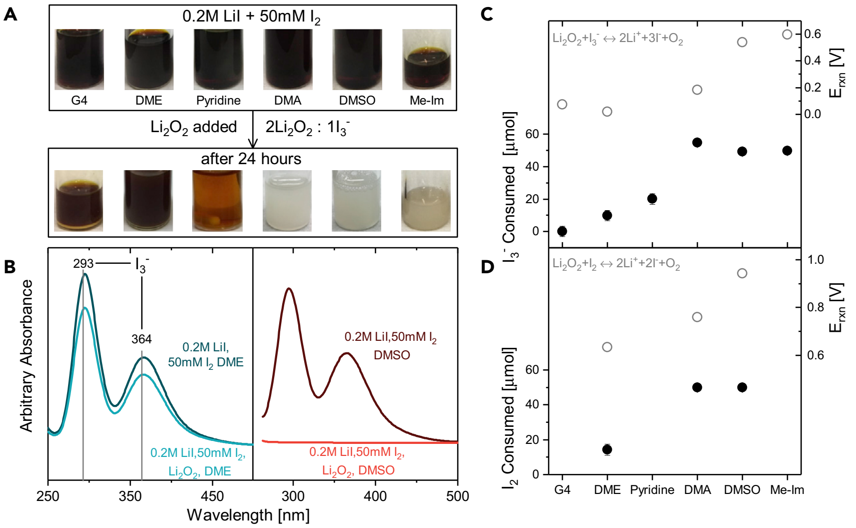

Figure 2. Solvent-Dependent Reaction between I_3^-/I^- and I_2/I_3^- and Li_2O_2

(A) Color changes when adding 1 mL of 50 mM I_3^- solution (50 µmol I_3^-) to 100 µmol of synthetic Li_2O_2 (Li_2O_2:I_3^- = 2:1) synthesized through disproportionation by adding 1 mL of 0.4 M LiTFSI (400 µmol LiTFSI) to KO_2 (200 µmol, LiTFSI:KO_2 = 2:1).

(B) UV-vis spectra of the liquid phase before and after the reaction with Li_2O_2 confirm the consumption of I_3^- in DMSO, but that I_3^- remains in DME.

(C) The consumption of I_3^- when adding 1 mL of 50 mM I_3^- solution (50 µmol I_3^-) to 100 µmol of synthetic Li_2O_2 (Li_2O_2:I_3^- = 2:1) (left axis, black filled symbols) measured after 24 h. I_3^- concentrations were determine through UV-vis spectroscopy. Full consumption of I_3^- was found in DMA, DMSO, and Me-Im with differences in the plot stemming from different initial amount. Error bars were estimated based on the accuracy of the mass balance used during preparation of diluted samples of ±0.5 mg. Calibration curves for each solvent can be found in Figures S8–S11. The difference between the I_3^-/I^- and $Li^+,O_2/Li_2O_2$ redox potentials (right axis, open gray symbols).

(D) The consumption of I_2 when adding 1 mL of 50 mM I_2 solution (50 µmol I_2) to 100 µmol synthetic Li_2O_2 (left axis, black filled symbols). The difference between the I_2/I_3^- and $Li^+,O_2/Li_2O_2$ redox potentials (right axis, open gray symbols).

The more oxidizing I_2 could fully oxidize Li_2O_2 in DMA and DMSO (Figure 2D) while only partially in DME after 24 h (Figure 2D). I_2 in DME could oxidize Li_2O_2 via $I_2 + Li_2O_2 \rightarrow 2Li^+ + 2I^- + O_2$, where the produced I^- could then associate with the remaining I_2 to form I_3^- ($I_2 + I^- \leftrightarrow I_3^-$), resulting in only partial consumption of the initial I_2 (Figures 2D and S15). Solutions of I_5^- (50 mM I_2 + 25 mM LiI) in DME also proceeded to oxidize Li_2O_2 until only I_3^- species remained (Figure S15), which was confirmed from Raman measurements of the decanted solution after 24 h of reaction (Figure S16). A discussion of higher-order polyiodide species (such as I_5^- and I_7^-) as well as the equilibrium between I_3^- and I_2 ($I_3^- \leftrightarrow I_2 + I^-$) is presented in the Supplemental Information. Reactions between commercial Li_2O_2 and $I_3^-/I_5^-/I_2$ in DME proceeded to a lesser extent than synthetic Li_2O_2 as shown in Figure S15, which can be attributed to (1) the oxygen-rich, defective surface of Li_2O_2 formed through disproportionation as reported previously,[61] and (2) the coverage of commercial Li_2O_2 particles with LiOH and/or Li_2CO_3.[62]

The oxidizing power of I_3^- against Li_2O_2 was found to not only be solvent-dependent but to also depend on the concentration of LiI present in the electrolyte through Nernstian shifts in the potentials of I_3^-/I^- and $Li^+,O_2/Li_2O_2$. CVs were collected in 0.5 M LiTFSI DME with 5, 10, 25, 50, and 100 mM of LiI with a Pt macroelectrode as the working electrode and Ag^+/Ag as the reference electrode (Figure S17A). The anodic peak of the I_3^-/I^- redox transition was found to exhibit a

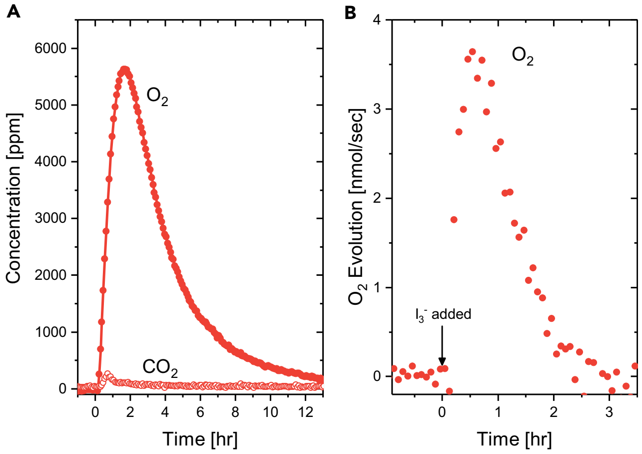

Figure 3. Gas Evolution when Li_2O_2 Is Oxidized to O_2 and Li^+ by I_3^-/I^- in DMSO

(A) Mass spectroscopy of the gas in the headspace of a sealed vial. At t = 0, 1.5 mL of 50 mM I_3^- DMSO solution (75 μmol I_3^-) is added to 50 μmol synthetic Li_2O_2 (Li_2O_2:I_3^- = 1:1.5) synthesized through disproportionation by adding 200 μmol LiTFSI to KO_2 (100 μmol, LiTFSI:KO_2 = 2:1). Carrier gas was argon and no signal from N_2 was detecting, indicating the absence of leaks.

(B) Measured O_2 evolution rate during the experiment.

Nernstian-type shift with the concentration of LiI present in the electrolyte (Figure S17B). The concentration-dependent oxidizing power of I_3^-/I^- toward Li_2O_2 was examined by adding 50 μmol I_3^- (1:1 LiI:I_2) to 100 μmol of synthetic Li_2O_2 (Li_2O_2:I_3^- = 2:1) synthesized through disproportionation by adding 400 μmol LiTFSI to KO_2 (200 μmol, LiTFSI:KO_2 = 2:1) and varying the concentration of I^- (as measured by the fully reduced form of all iodide species added) by changing the amount of DME added to the reaction vessel in order to generate Nernstian shifts in both the I_3^-/I^- redox transition (Figure S17B) as well as the Li^+,O_2/Li_2O_2 potential through the dilution of Li^+ in the electrolyte. Quantification of the consumption of I_3^- through UV-vis spectroscopy (Figures S17C and S18) revealed that by shifting the I_3^-/I^- potential to higher potentials and the Li^+,O_2/Li_2O_2 potential to lower potentials through dilution of the reaction with pure DME, the oxidizing power of I_3^- toward Li_2O_2 could be increased, leading to a doubling of the consumption of I_3^- during the reaction (Figure S17D) from 100 mM to 5 mM I^-.

No solvent decomposition was detected for G4, DME, and DMA, whereas decomposed species from pyridine, DMSO, and Me-Im were found in the presence of Li_2O_2 and/or I_3^-. ^{1}H NMR measurements of the solution phase decanted from the reaction mixture after 24 h were used to detect protonated species produced after the addition of synthetic Li_2O_2. No changes were observed in G4, DME, and DMA (Figure S19), indicating no detectable solvent decomposition. On the other hand, a small peak at ~2.95 ppm appeared for DMSO, indicative of dimethyl sulfone ($DMSO_2$)[63] as shown in Figure S20, which was quantified to be ~6 μmol. This observation is in agreement with previous work showing that DMSO is chemically unstable in the presence of Li_2O_2-like and LiO_2 species.[63,64] In addition, changes were found for the ^{1}H NMR peaks of Me-Im at ~7.1 ppm (splitting into two peaks) and ~7.7 ppm (shifting downfield) (Figure S19), which can be attributed to altered Me-Im proton exchange dynamics caused by the introduction of a Brønsted base (I^-/I_3^-).[65] This hypothesis is supported by comparable changes found when a solution of I_3^- was prepared in Me-Im (without addition of Li_2O_2 as shown in Figure S21). Strong interactions between iodide species and Me-Im can lead to the iodination of Me-Im,[66] which is in agreement with the observed color-fading of I_3^- in Me-Im over time in

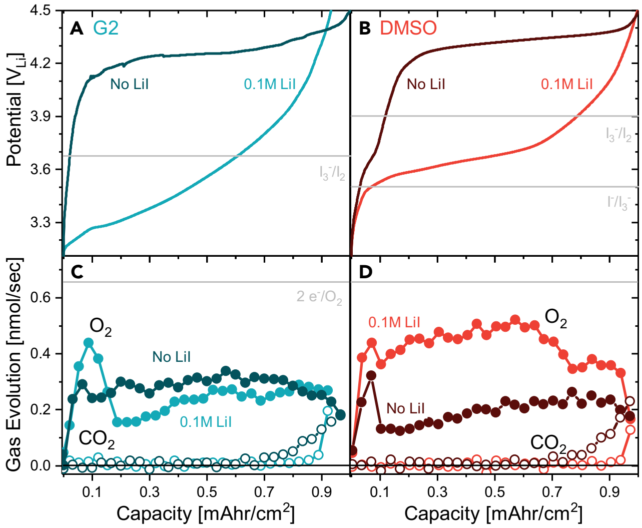

Figure 4. DEMS during Charging of Li-O_2 Cells with G2/DMSO

(A–D) Voltage profile and corresponding O_2 (filled) and CO_2 (open) evolution during charge at 0.1 mA/cm^2 in 0.5 M LiTFSI in G2 (A and C) or DMSO (B and D), both with 0.1 M LiI (lighter colors) and with an additional 0.1 M LiTFSI (darker colors) to keep the overall [Li^+] constant. Cells were constructed with a Li-metal counter electrode and a solid Li-conducting separator to prevent shuttling of oxidized iodide species from the positive electrode to the Li-metal electrode where they can be chemically reduced and diffuse back to the positive electrode.[44] Potentials are referenced against the Li-metal counter electrode. Cells were first discharged for 20 h at 0.05 mA/cm^2 under O_2 environment, and then the cell headspace was evacuated and purged with argon gas five times. The added 0.1 M LiI could provide a theoretical maximum of 33 mM I_3^- and 50 mM I_2, accounting for a maximum of 0.25 mAh/cm^2 of capacity.

diluted samples for UV-vis analysis (Figure S22). Considering the short duration of Li_2O_2 oxidation (<10 s) by I_3^- and long iodination reaction time (>weeks for a 50 mM solution without Li_2O_2) required to render colorless solutions, the oxidation of Li_2O_2 by I_3^- to form I^- dominates.

DEMS measurements during charging of Li-O_2 cells with and without LiI following the first discharge revealed an enhancement in oxygen evolution in DMSO with LiI addition but no enhancement in diglyme (G2). DEMS cells were assembled using 0.5 M LiTFSI in G2 or DMSO, with and without 0.1 M LiI, where shuttling was suppressed using a solid Li-conducting separator. G2 was selected instead of DME and G4 as it has a higher vapor pressure than DME and lower viscosity than G4 but similar solvation properties as supported by CV measurements (Figure S1; Table S1) and tabulated solvent viscosities from literature (Table S2). Cells were first discharged at 0.05 mA/cm$^2_{geo}$ for 20 h to yield 1 mAh/cm^2 of capacity, after which only Li_2O_2 was detected by XRD (Figure S23). The addition of LiI markedly reduced the charging potential in both solvents (Figures 4A and 4B) while it did not lead to significant changes in the discharge voltage. Unfortunately, despite considerable capacity below the I_2/I_3^- redox transition, DEMS measurements showed a slight decrease in the oxygen evolution rate with the addition of LiI on charge in G2 (Figure 4C). This capacity below the I_2/I_3^- redox transition during charging in G2 can be attributed to three sources: (1) 0.25 mAh/cm^2 of capacity is required to fully oxidize the I^- in the electrolyte to I_2, (2) I_3^- was found to be partially reactive with synthetic Li_2O_2 in DME (Figure 2C), consuming ~15% of the Li_2O_2 which could reasonably account for ~0.15 mAh/cm^2 of capacity and explain the sharp rise in O_2 evolution observed at the beginning of charge, and (3) direct electrochemical of Li_2O_2 is possible at potentials below I_2/I_3^- and could account for the remaining ~0.2 mAh/cm^2 needed to explain the ~0.6 mAh/cm^2 of capacity observed. On the other hand, the addition of LiI in DMSO led to greater (~ two times) rates of oxygen evolution during charge relative to that without LiI, which was accompanied with a plateau-like profile (~ 3.7 V_{Li}) in between the redox potentials of I_3^-/I^- (~3.5 V_{Li}) and I_2/I_3^- (~3.9 V_{Li}) as shown in Figure 4D. This observation further supports that having the I_3^-/I^- redox potential greater than that of $Li^+,O_2/Li_2O_2$ in solvents such as DMSO can facilitate Li_2O_2 oxidation to evolve O_2, while those equal to or lower than $Li^+,O_2/Li_2O_2$ in solvents such as G2 and DME are unable to promote the oxidation of Li_2O_2. More work is needed to better understand the isolated influences of ionic conductivity, electroxidation kinetics of the redox mediator, reaction kinetics between the oxidized redox mediator and Li_2O_2 as well as redox mediator mass transport effects on the total cell overpotential during charge, but such an investigation is beyond the scope of this paper. We note that the difference between the I_2/I_3^- potential on a Li^+/Li scale presented in Figure 4 (~3.7 V_{Li} in G2 and ~3.9 V_{Li} in DMSO) stems from the difference in the Li^+/Li potential versus $Me_{10}Fc$ in G2 and DMSO because of the stronger solvation of Li^+ in DMSO.

Solvent-Dependent Oxidizing Power of I_3^-/I^- and I_2/I_3^- toward LiOH

The reaction between I_3^- and LiOH was found to be solvent dependent, with I_3^- being fully consumed in DMA, DMSO, and Me-Im but little to no reaction occurring in G4, DME, and pyridine. The solvent-dependent oxidizing power of I_3^-/I^- toward LiOH was examined by adding commercial LiOH (0.2 μmol, LiOH:I_3^- = 4:1) to 1 mL of 50 mM I_3^- (50 mM I_2 + 0.2 M LiI, $I^-:I_2$ = 4:1) in different solvents. The brown-colored solution became clear in DMA (~48 h), DMSO (~1 h), and Me-Im (~10 min). This color change could be attributed to the reduction of I_3^- (dark brown) to I^- (colorless) as revealed by UV-vis spectroscopy of the liquid phase decanted from the reaction mixture after 48 h (Figures 5A and S24). On the other hand, no color change was found for pyridine, DME, and G4 after 48 h as evidenced by the characteristic peaks for I_3^- at 293 nm and 364 nm remaining after the reaction with LiOH (Figures 5A and S24). The consumption of I_3^- after the reaction for 48 h was quantified using the absorbance of I_3^- with known concentrations (Figures S8–S11). All the I_3^- was consumed in DMA, DMSO, and Me-Im while nearly no I_3^- was consumed in G4, DME, and pyridine, as shown in Figure 5A. Similarly, as shown in Figure 5B, the addition of LiOH to the more oxidizing I_2 in DMA and DMSO led to complete consumption of I_2 while in DME, the reaction stopped after only I_3^- remained (Figures 5B and S25), resulting from the previously discussed association between I^- generated by the reaction and the remaining I_2 via $I_2 + I^- \leftrightarrow I_3^-$. Anhydrous LiOH synthesized via the disproportionation of KO_2 in a two times excess of LiTFSI in MeCN with added water (Figure S26) was found to exhibit similar reactivity to commercial anhydrous LiOH in the presence of I_3^-, with a brown-colored 50 mM I_3^- solution becoming clear in DMA (~96 h) and DMSO (~1 h), but no visible color change in DME after 96 h (Figure S27).

Unfortunately, the reaction between I_3^- and anhydrous LiOH in solvents such as DMSO did not yield oxygen evolution as shown from GC measurements with commercial LiOH (Figure S28) and mass spectrometry with synthetic LiOH (Figure S29). As expected, because of the excess of LiOH (LiOH:I_3^- = 4:1), Raman spectra of the solid recovered after the reaction between LiOH and I_3^- in all solvents revealed anhydrous LiOH as the dominant phase remaining after the reaction (Figure S30). To further probe potential solid reaction products between I_3^- and LiOH, the I_3^- excess reaction with commercial anhydrous LiOH (LiOH:I_3^- = 1:1) in DMSO was performed for more than 1 week. Raman (Figure 5C) and XRD (Figure S31) of the solid

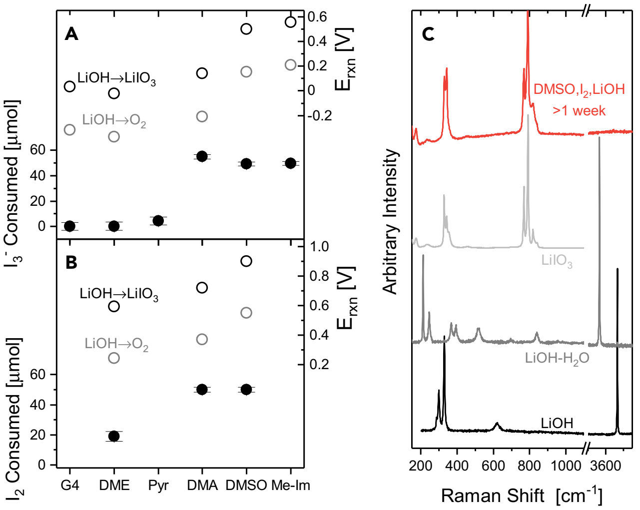

Figure 5. Solvent-Dependent Reaction between I_3^-/I^- and I_2/I_3^- and LiOH

(A) The consumption of I_3^- when adding 200 μmol of commercial LiOH to 1 mL of 50 mM I_3^- solution (50 μmol I_3^-, LiOH:I_3^- = 4:1) (left axis, black filled symbols) measured after 48 h. I_3^- concentrations were determine through UV-vis spectroscopy. Full consumption of I_3^- was found in DMA, DMSO, and Me-Im with differences in the plot stemming from different initial concentrations. Error bars were estimated based on the accuracy of the mass balance used during preparation of diluted samples of ±0.5 mg. Calibration curves for each solvent can be found in Figures S8–S11. The difference between the I_3^-/I^- and $Li^+,O_2,H_2O/LiOH$ redox potentials (right axis, open gray symbols) and $Li^+,IO_3^-,H_2O/LiOH,I^-$ redox potentials (right axis, open black symbols).

(B) The consumption of I_2 when adding 200 μmol of commercial LiOH to 1 mL of 50 mM I_2 solution (50 μmol I_2, LiOH:I_3^- = 4:1) (left axis, black filled symbols) measured after 48 h. The difference between the I_2/I_3^- and $Li^+,O_2,H_2O/LiOH$ redox potentials (right axis, open gray symbols) and $Li^+,IO_3^-,H_2O/LiOH,I^-$ redox potentials (right axis, open black symbols).

(C) Raman spectra of the solid precipitate, which was separated and washed after reacting an excess of I_2 with LiOH in DMSO and three reference spectra ($LiIO_3$, LiOH, and LiOH-H_2O). The solid precipitate has only peaks consistent with $LiIO_3$ and no erroneous peaks; measurement is representative of three separate locations in the solid.

recovered revealed $LiIO_3$ only without LiOH remaining. The presence of $LiIO_3$ has been previously reported by Burke et al.[44] upon charging of cells having LiOH formed during discharge with LiI in DME. The formation of $LiIO_3$ can come from the following reaction: $3I_3^- + 6LiOH \rightarrow 8I^- + 5Li^+ + 3H_2O + LiIO_3$, which can include the reaction between I_3^- and LiOH to generate hypoiodite ($I_3^- + 2LiOH \rightarrow 2I^- + 2Li^+ + H_2O + IO^-$) and the disproportionation of hypoiodite (IO^-) to iodate IO_3^-[67–69] ($3IO^- \rightarrow 2I^- + IO_3^-$). The presence of IO^- is supported by the presence of a vibration at 430 cm^{-1} previously attributed to IO^-[70] (Figure S32) by *in situ* Raman spectroscopy of a solution of commercial anhydrous LiOH with I_3^- in DMSO. The thermodynamic driving force to form $LiIO_3$ from LiOH ($3I_3^- + 6LiOH \rightarrow 8I^- + 5Li^+ + 3H_2O + LiIO_3$) is much greater than that for oxygen evolution ($2I_3^- + 4LiOH \rightarrow 6I^- + 4Li^+ + 2H_2O + O_2$), and increases with greater redox potentials of I_3^-/I^- on the Li^+/Li scale from G4/DME, to DMA, to DMSO, to Me-Im (Figure 5A). The Gibb's free energy of formation of $LiIO_3$ was not available in literature but could be approximated as detailed in the Supplemental Information. Of particular significance is the case of DMA, where full consumption of I_3^- was observed and the reaction to form $LiIO_3$ is predicted to be spontaneous ($E_{rxn} = -\Delta G_{rxn}/6F = +0.17V$) whereas the reaction to form O_2 is not ($E_{rxn} = -\Delta G_{rxn}/4F = -0.21V$), which further supports the preference for $LiIO_3$ formation instead of O_2 evolution. Similar trends were found for I_2/I_3^- where increased thermodynamic driving force correlated with increased consumption of I_2 in DME, DMA, and DMSO (Figure 5B).

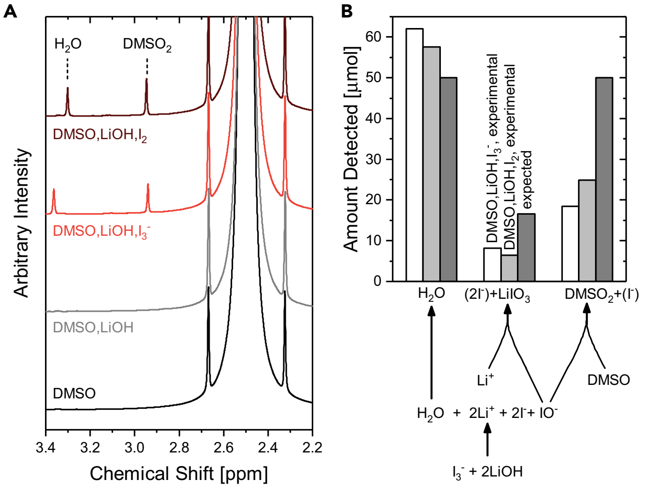

Figure 6. I_2/I_3^- Reacts with LiOH to Form IO^- in DMSO

(A) ^{1}H NMR spectrum of pure DMSO, DMSO after exposure to LiOH, and DMSO after the reaction between 50 mM I_2/I_3^- and 200 μmol commercial LiOH (LiOH:I_2/I_3^- = 4:1). After the reactions between I_2/I_3^- and LiOH, two new peaks appear; one at ~2.95 ppm (based on the DMSO peak being assigned to 2.5 ppm) corresponding to DMSO$_2$ and one at ~3.3 ppm corresponding to H_2O. All ^{1}H NMR samples were prepared by mixing 0.5 mL of the sample + 0.1 mL of DMSO-D6 (for NMR locking) + 10 μL of 1,4-dioxane internal reference (for quantification).

(B) Full quantification of detected liquid and solid products after reactions between I_2/I_3^- and LiOH. $LiIO_3$ was quantified using iodometric titration, DMSO$_2$ and H_2O were quantified using ^{1}H NMR with an internal standard of 1,4-dioxane.

Quantifications through ^{1}H NMR analysis of the solution phase and iodometric titration after reaction with 50 mM I_3^-/I_2 further confirmed the proposed reaction mechanism for the formation of $LiIO_3$. An H_2O peak became visible following the addition of LiOH to DMA (Figure S19), DMSO (Figures 6A and S19), and Me-Im (Figure S19) with 50 mM I_3^- for 48 h. No H_2O was detected in the liquid phase from mixing DMSO (without oxidized iodide species) with LiOH, while an H_2O peak at 3.36 and 3.30 ppm was detected after reacting LiOH with 50 mM I_3^- and 50 mM I_2 in DMSO, respectively (Figure 6A). The upfield shift of H_2O found for I_2 compared to I_3^- can be attributed to the larger quantity of I^- in the solution following the reaction with I_3^-, as shown previously for changes in the ^{1}H NMR chemical shift of H_2O induced by interactions with I^- in DME.[45] In contrast, no H_2O or other changes were observed in the ^{1}H NMR spectra of G4 and DME (Figure S19) following the reaction between LiOH and I_3^- while pyridine showed the emergence of some small peaks (Figure S19), which we attribute to solvent decomposition. In addition to the formation of H_2O, reactions between LiOH and I_3^-/I_2 in DMSO resulted in DMSO$_2$ (~2.95 ppm, Figure S20) with quantities of 18 μmol and 25 μmol for reactions with I_3^- and I_2, respectively (Figures 6A and 6B) while Me-Im experienced peak changes (Figures S19 and S21), which can be attributed to the previously discussed interactions with I^-/I_3^-.[66] The amount of iodate species detected with iodometric titration (8.2 μmol and 6.4 μmol for reactions with I_3^- and I_2 in DMSO, respectively) was close to that expected (16.7 μmol) for $3I_3^- + 6LiOH \rightarrow 8I^- + 5Li^+ + 3H_2O + LiIO_3$, as shown in Figure 6B. The difference can be attributed to the decomposition of DMSO by an IO^- intermediate via $IO^- + (CH_3)_2SO \rightarrow I^- + (CH_3)_2SO_2$, which accounts for 18.5/24.9 μmol of IO^- consumed in reactions with I_3^- and I_2, respectively, which otherwise could have disproportionated to form $LiIO_3$. A similar oxidation of DMSO to DMSO$_2$ from intermediates of LiOH oxidation was reported by Liu et al.[71] in a ruthenium-catalyzed Li-O_2 battery system. Therefore, combined spectroscopic data from ^{1}H

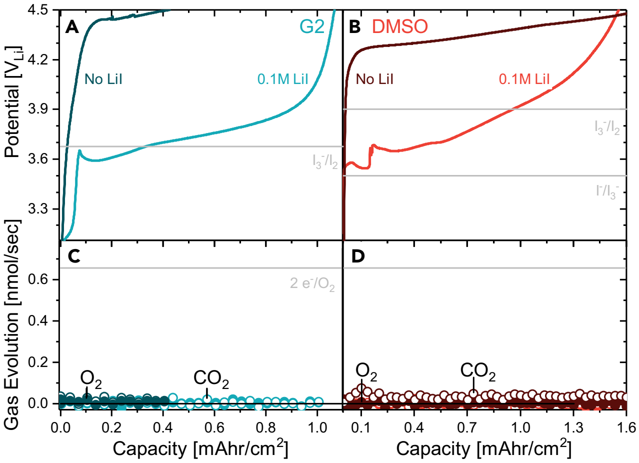

Figure 7. DEMS during Charging of LiOH Pre-loaded Electrodes with G2/DMSO

(A–D) Voltage profile and corresponding O_2 (filled symbols) and CO_2 (open symbols) evolution during charge of LiOH pre-loaded electrodes at 0.1 mA/cm^2 in 0.5 M LiTFSI in G2 (A and C) or DMSO (B and D), both with 0.1 M LiI (lighter colors) and with an additional 0.1 M LiTFSI (darker colors) to keep the overall [Li$^+$] constant. Cells were constructed with a Li-metal counter electrode and a solid Li-conducting separator to prevent shuttling of oxidized iodide species from the positive electrode to the Li-metal electrode where they can be chemically reduced and diffuse back to the positive electrode.[44] Potentials are referenced against the Li-metal counter electrode. The added 0.1 M LiI could provide a theoretical maximum of 33 mM I_3^- and 50 mM I_2, accounting for a maximum of 0.25 mAh/cm^2 of capacity.

NMR, Raman, GC, and iodometric titration show that the reaction between LiOH and oxidized iodide species such as I_3^- leads to the formation of an IO^- intermediate, which can disproportionate to form $LiIO_3$ as the major product and attack solvent molecules to form species such as $DMSO_2$. This reaction mechanism does not lead to the formation of O_2 gas as some have reported previously.[15,48]

The proposed reaction mechanism of LiOH in the presence of oxidized iodide species is supported by galvanostatic charging and DEMS measurements (Figure 7) of pre-loaded commercial, anhydrous LiOH electrodes with a solid Li-conducting separator to eliminate shuttling, charged in 0.5 M LiTFSI G2 (Figures 7A and 7C) and DMSO (Figures 7B and 7D) with and without 0.1 M LiI addition (in cases where no LiI was added, an additional 0.1 M LiTFSI was added to fix the total Li$^+$ concentration at 0.6 M). Of significance, there was no observable oxygen generation in either G2 or DMSO, which supports the proposed reaction with LiOH by oxidized iodide species to form $LiIO_3$. The majority of the charging plateau took place above the I_3^-/I_2 redox transition in G2 (comparable to DME/G4), indicating that I_3^- could not react with LiOH in glymes but I_2 could, which is consistent with *ex situ* chemical reactions (Figures 5A and 5B). On the other hand, significant capacity was noted below the I_3^-/I_2 redox transition in DMSO, corresponding to the formation of $LiIO_3$ from I_3^-. XRD of the electrodes after charging (Figure S33) indicated that not all LiOH was removed, which is consistent with the calculated charging capacity based on the mass of deposited LiOH (7.3 and 5.2 mAh/cm^2 for G2 and DMSO, respectively) being considerably higher than the achieved charging capacity (1.0 and 1.6 mAh/cm^2 for G2 and DMSO, respectively). However, the observed capacity is significantly larger than the maximum calculated capacity based on the oxidation of LiI (~0.25 mAh/cm^2), indicating consumption of LiOH during charge. We postulate the incomplete oxidation of LiOH *in situ* may relate to either slow kinetics of reaction with LiOH by oxidized iodide species (shown to be much slower than the oxidation of

Li_2O_2 in *ex situ* experiments; Figure S34) and/or the passivation of the LiOH surface by insoluble $LiIO_3$. Leftover LiOH after charging is consistent with the observations of Qiao et al.[46]; however, using *ex situ* reactions and a solid Li-conducting separator to eliminate shuttling, we are able to demonstrate that LiOH is still active during the charging process and not inactive as suggested by Qiao et al.[46]

DISCUSSION

The oxidation of Li_2O_2 by oxidized iodide species leads to O_2 gas evolution whereas anhydrous LiOH reacts irreversibly to form IO^-, which can then either disproportionate to form $LiIO_3$ or attack solvent molecules. Thermodynamic calculations based on the oxidizing power of I_3^- in DME reveal that the formation of $LiIO_3$ is always thermodynamically preferred to O_2 evolution: the reaction between I_3^- and Li_2O_2 to form $LiIO_3$ ($I_3^- + Li_2O_2 \rightarrow \frac{7}{3}I^- + \frac{4}{3}Li^+ + \frac{2}{3}LiIO_3$, $\Delta G_{rxn} \sim -0.8$ eV) is thermodynamically preferred to the reaction between I_3^- and Li_2O_2 to form O_2 ($I_3^- + Li_2O_2 \rightarrow 3I^- + 2Li^+ + O_2$, $\Delta G_{rxn} \sim 0.0$ eV). Similarly, the reaction between I_3^- and LiOH to form $LiIO_3$ ($\frac{1}{2}I_3^- + LiOH \rightarrow \frac{8}{6}I^- + \frac{5}{6}Li^+ + \frac{1}{2}H_2O + \frac{1}{6}LiIO_3$, $\Delta G_{rxn} \sim 0.0$ eV) is thermodynamically preferred to the reaction between I_3^- and LiOH to form O_2 ($\frac{1}{2}I_3^- + LiOH \rightarrow \frac{3}{2}I^- + Li^+ + \frac{1}{2}H_2O + \frac{1}{4}O_2$, $\Delta G_{rxn} \sim +0.4$ eV). Since $LiIO_3$ is thermodynamically favorable to form from both Li_2O_2 and LiOH, it is proposed that the evolution of O_2 without the formation of $LiIO_3$ upon oxidation of Li_2O_2 by oxidized iodide species can be attributed to slow kinetics of O-O dissociation needed to form IO^- and subsequently $LiIO_3$, which is supported by the shorter O-O distance in the Li_2O_2 lattice (1.53Å[72] compared with 3.05Å[73] for LiOH). Further support for this hypothesis came from experiments with KO_2 and Li_2O, where the O-O distance in the lattice is 1.28 Å[74] and 3.32 Å,[75] respectively. For reactions between KO_2 and Li_2O and I_3^- in DME, the formation of iodate, $\frac{1}{2}I_3^- + KO_2 \rightarrow \frac{5}{6}I^- + \frac{1}{3}K^+ + \frac{2}{3}KIO_3$ ($\Delta G_{rxn} \sim -1.6$ eV) is again thermodynamically preferred to $\frac{1}{2}I_3^- + KO_2 \rightarrow \frac{3}{2}I^- + K^+ + O_2$ ($\Delta G_{rxn} \sim -0.4$ eV), and $I_3^- + Li_2O \rightarrow \frac{8}{3}I^- + \frac{5}{3}Li^+ + \frac{1}{3}LiIO_3$ ($\Delta G_{rxn} \sim -0.9$eV) is thermodynamically preferred to $I_3^- + Li_2O \rightarrow 3I^- + 2Li^+ + \frac{1}{2}O_2$ ($\Delta G_{rxn} \sim -0.1$ eV). Despite this thermodynamic preference for iodate, the oxidation of KO_2 (with an O-O distance of 1.28 Å[74]) by I_3^- in G2 was found to readily evolve O_2 using DEMS (Figures S35 and S36). On the other hand, the chemical reaction between Li_2O (with an O-O distance of 3.32 Å[75]) and 50 mM I_3^- in DMSO led to $LiIO_3$ as detected by Raman and XRD (Figure S37). While not conclusive, reactions between KO_2, Li_2O_2, LiOH, and Li_2O, and I_3^- are consistent with our hypothesis that when the O-O lattice distance is small (1.28 Å[74] and 1.53Å[72] for KO_2 and Li_2O_2, respectively), reactions with I_3^- produce O_2 because of a kinetic barrier to IO^- formation, whereas when the O-O lattice distance is large (3.05Å[73] and 3.32 Å[75] for LiOH and LiO_2, respectively), reactions with I_3^- produce the thermodynamically preferred $LiIO_3$.

In this work, the role of LiI on the charging process of Li-O_2 batteries was examined by systemically studying the solvent-dependent oxidizing power of I_3^-/I^- and I_2/I_3^- toward Li_2O_2 and LiOH. The oxidizing power of I_3^-/I^- and I_2/I_3^- toward Li_2O_2 and anhydrous LiOH was probed chemically by examining the consumption of I_3^- upon addition of synthetic Li_2O_2, where the liquid reaction product was examined using UV-vis spectroscopy and ^{1}H NMR, the solid reaction products were studied by Raman spectroscopy and XRD, and the gaseous products were assessed using gas chromatography and mass spectroscopy. In addition, the role of I^- on the charging of Li-O_2 batteries and commercial anhydrous LiOH pre-loaded cells was examined using DEMS, where the amount of oxygen generated was quantified. We have shown that I_3^-/I^- shifts toward higher potentials in solvents with higher dielectric constant and AN, suggesting stronger solvation of I^- ions, whereas the

I_2/I_3^- potential was observed to be largely solvent independent in the considered solvents. This strong solvation of I^- ions, coupled with a strong solvation of Li^+ ions in solvents such as DMA, DMSO, and Me-Im was found to increase the oxidizing power of I_3^-/I^- against insoluble Li_2O_2, allowing I_3^- to effectively oxidize Li_2O_2 to generate O_2, which was supported by chemical and electrochemical experiments. In solvents with weaker solvation of I^- and Li^+ (such as DME and G4), the more oxidizing I_2/I_3^- redox couple was needed before Li_2O_2 could be fully oxidized to O_2. The reaction between anhydrous LiOH and I_3^- was also found to be solvent dependent, where no reaction was observed in G4, DME, and pyridine while the reaction proceeded to completion in DMA, DMSO, and Me-Im where the I_3^-/I^- redox potential was above ~3.1 V_{Li}. No O_2 was detected from the reaction between LiOH and I_3^- using gas chromatography, mass spectroscopy, or during charging of preloaded LiOH electrodes in DEMS but instead the reaction between LiOH and I_3^- was found to produce water and a hypoiodite (IO^-) intermediate, which could either disproportionate to form $LiIO_3$ or attack solvent molecules and result in decomposition products such as dimethyl sulfone ($DMSO_2$). We propose that the selectivity between O_2 and the thermodynamically preferred $LiIO_3$ is governed by a kinetic barrier relating to O-O bond dissociation and this kinetic barrier prevents IO^- formation, allowing for the evolution of gaseous O_2 when oxidizing Li_2O_2, which was supported by reactions between oxidized iodide species and KO_2 and Li_2O. The previously reported formation of LiOH from even trace amounts of water in the presence of LiI,[45] coupled with the finding presented in this work that LiOH reacts irreversibly with oxidized iodide species to form $LiIO_3$ indicate that LiI might not be a suitable soluble redox mediator for facilitating the charging process in Li-O_2 batteries.

EXPERIMENTAL PROCEDURES

Chemicals

High purity dimethyl sulfoxide (DMSO, Sigma-Aldrich, anhydrous, ≥99.9%), diethylene glycol dimethyl ether (G2, Sigma-Aldrich, anhydrous, 99.5%), N,N-dimethylacetamide (DMA, Sigma-Aldrich, anhydrous, 99.8%), 1-methylimidazole (Me-Im, Sigma-Aldrich, 99%), pyridine (Sigma-Aldrich, anhydrous, 99.8%), and tetraethylene glycol dimethyl ether (G4, Sigma-Aldrich, ≥99%) were purchased and dried over molecular sieves for at least a week before use. 1,2-dimethoxyethane (DME) was purchased from Acros and was degassed and dried using a Glass Contour Solvent Purification System built by SGWater USA, LLC. Lithium bis(trifluoromethanesulfonyl) imide (LiTFSI, 99.99% extra dry grade kindly provided by Solvay) was used as received. High purity LiI (ultra dry, 99.999% pure), I_2 (99.9985% pure), Li_2O_2 (90%), Li_2O (99.5%), and decamethylferrocene ($Me_{10}Fc$, 99%) chemicals were ordered from Alfa Aesar and were used as received. LiOH (anhydrous, 99.995%) was purchased from Alfa Aesar and was further dried under vacuum for 24 h at 170°C to ensure only the anhydrous phase remained (see Figure S38). KO_2 (99% pure) powder was purchased from Sigma-Aldrich and was used as received.

All chemicals were stored in an argon-filled glovebox (MBraun, USA) with H_2O and O_2 content of <0.1 ppm. Electrolytes were prepared by dissolution of a desired amount of salts in the solvent with molarity determined by the volume of solvent added. The total H_2O content in the solvents and electrolytes was checked using a C20 compact Karl Fisher coulometer from Mettler Toledo and for the dry solvent it was <20 ppm for ~2 g of sample. A 20 wt% solution of LiTFSI in DME was found to have a slightly higher water content of 21 ppm (compared with 3.0 ppm for the pure DME solvent). Solutions of 0.2 M LiI in all solvents were colorless, indicating the absence of H_2O_2 contamination, which can be of particular concern in glymes.

Due to the low purity of commercially available Li_2O_2 (90%), for most experiments, Li_2O_2 was first synthesized through the well-known disproportionation reaction between KO_2 and Li-containing salt[4]:

$$2LiTFSI + 2KO_2 \rightarrow 2KTFSI + Li_2O_2 + O_2. \qquad \text{(Equation 1)}$$

In all experiments, a two times excess of LiTFSI was used, the reaction occurred in the solvent being studied and the reaction was allowed to proceed for 1 h with stirring to ensure complete production of Li_2O_2. The resulting solution of unconsumed LiTFSI and produced KTFSI as well as the precipitated Li_2O_2 was used directly without additional processing or washing. The presence of LiTFSI and KTFSI was assumed to have a negligible influence on subsequent reactions, the amounts of which were the same in all solvents studied.

Similarly, for some experiments, synthetic anhydrous LiOH was used. Anhydrous LiOH was synthesized to have representative morphology to that which might form in a Li-O_2 cell during discharge. To achieve this, the disproportionation between KO_2 and LiTFSI was carried out in MeCN with added water. Previous studies have showed that the solvent-water interactions in MeCN facilitate the deprotonation of water, leading to LiOH instead of Li_2O_2 during discharge when 5,000 ppm H_2O is present.[49] The recovered solid was then washed in DME, and Raman spectroscopy confirmed anhydrous LiOH as the dominant phase (Figure S26).

Redox Potential Measurements of I_3^-/I^- and I_2/I_3^- Redox Couples Using Cyclic Voltammograms

Cyclic voltammograms (CVs) were collected with solutions of 0.5 M LiTFSI + 10 mM LiI at 100 mVps under argon environment in each of the considered solvents. Electrolytes were prepared in an Argon-filled glove box (MBraun, <0.1 ppm H_2O, <0.1 ppm O_2) and transferred to a second Argon-filled glovebox (MBraun, <0.1 ppm H_2O, <0.1% O_2) directly through a shared antechamber. The electrolyte was bubbled with Argon for at least 30 min prior to beginning electrochemistry. As a result of the volatility of DME, for the DME experiment, the Argon was first saturated with DME vapor by bubbling the Argon through pure DME prior to going to the electrolyte. The working macroelectrode was platinum and either a Li metal (G4, DME, or DMSO) or lithium titanium oxide (pyridine, DMA, or Me-Im) counter electrode was used. A fritted Ag/Ag^+ reference electrode (0.1 M $TBAClO_4$ + 10 mM $AgNO_3$ in MeCN) was used and following collection of CVs, 2 mM $Me_{10}Fc$ was added to the solution and CVs were collected to determine the $Me_{10}Fc$ half-wave potential. Li^+/Li potentials were determined in G4, G2, DME, DMA, and DMSO using a piece of Li metal at OCV. The Li^+/Li potential in Me-Im was approximated using the Li-stripping potential on a Pt macroelectrode as per Kwabi et al.[6] (Figure S39). Unfortunately, the Li^+/Li potential for pyridine could not be reliably extracted with this method (Figure S39).

In addition to the two expected peaks associated with the I^-/I_3^- and I_3^-/I_2 redox transitions, both pyridine and Me-Im exhibit additional redox features (Figure S1). Pyridine is known, as suggested in the literature, to form stable complexes with oxidized forms of iodide[76,77] as well as adsorb strongly on platinum surfaces.[78] We therefore attribute the small peak at ~ -0.35 V versus $Me_{10}Fc$ to a desorption process (total charge passed $\sim 1.2\times10^{-7}$ C) and the additional features in the I_3^-/I^- and I_2/I_3^- redox peaks to the formation of iodine-solvent complexes. Given the similarities in structure between Me-Im and pyridine, we suggest that similar iodine-solvent complexes are also possible in Me-Im and would account for the additional feature observed in the anodic sweep of the Me-Im CV. Since neither pyridine nor

Me-Im are likely solvent candidates for lithium oxygen batteries because of instability issues, the precise origin and implications of these additional redox features in the presented CVs was not investigated further.

Using I_3^-/I^- and I_3^-/I_2 for Chemical Reactions with Li_2O_2 and LiOH

In an argon-filled glovebox (*MBraun*, O_2, $H_2O < 0.1$ ppm), solutions of I_3^- (0.2 M LiI + 50 mM I_2) and I_2 (50 mM I_2) were first prepared in each solvent and allowed to fully dissolve under stirring. For studies of Li_2O_2, a two times excess of Li_2O_2 was first synthesized through disproportionation using 1 mL of the solvent to be studied and the reaction was allowed to proceed under stirring for ~1 h. For studies of LiOH, a two times excess of LiOH powder was added to 1 mL of solvent and allowed to reach equilibrium under stirring for ~1 h. Next, 1 mL of the I_3^-/I_2 solution was added to the vial with Li_2O_2/LiOH and 1 mL of solvent. The reaction was allowed to take place under stirring for 24 h, following which, the solid product was allowed to settle for 1 h and the liquid and solid phases were separated. This *ex situ*, chemical analog approach has been used extensively previously[44,45,48,79] and has been very effective at isolating a chemical reaction to enable its independent study.

Physical Characterization of Reaction Liquids, Solids, and Gases

UV-vis was performed using a PerkinElmer Lambda 1050 UV/VIS/NIR Spectrophotometer. The pure solvent (e.g., G4, DME, etc.) was used as the blank solution, except in assessments of the pure solvent absorbance (Figure S40) where no blank was used. Solutions were prepared in an Argon glovebox and sealed in a quartz cuvette used for data collection, preventing air exposure. As a result of the high molar absorptivity of I_3^-, the solutions with I_3^- were diluted in pure solvent so that the intensity of I_3^- absorption signals (at ~293 nm and ~364 nm) were within the calibration range (Figures S8–S11). The concentrations of triiodide were calculated based on the absorption intensity at the wavelength of the highest absorbance of the calibration curves. In the case where both peaks were distinguishable above the solvent's inherent absorbance (Figure S40), the average of the concentration determined by both peaks was used. The absorption spectra in the figures are rescaled (arbitrary units) in order to visualize the difference in I_3^- concentration for different solutions. Thus, a high concentration of I_3^- corresponds to high absorption at wavelengths 293 nm and 364 nm and vice versa. The scale factors and the calculation of I_3^- concentrations are summarized in Table S3. Dilutions were calculated based on a mass balance of the added solvent and I_3^- solution. Error bars for the diluted samples were estimated based on an error of ±0.5 mg in each weight measurement (±0.1 mg from the accuracy of the balance with additional error incurred because of a small amount of evaporation). In the case of determining the concentration of I_2 in solution, the solution was first mixed with a ~4 times excess of LiI to chemically form I_3^- in solution through the association of I_2 and I^-. The resulting I_3^- concentration was then determined using the procedure as described above.

Iodometric titration was performed with a prepared 5 mM thiosulfate solution (anhydrous 99.99% Sigma-Aldrich, stored in desiccator) using a 50 mL burette (class A, graduation 0.10 mL, tolerance ± 0.05 mL from VWR) and starch indicator (1% w/v of amylodextrin) in aqueous solution (18.2 MΩ•cm, Millipore). The thiosulfate solution was first standardized with a KIO_3 (99.995% pure from Sigma-Aldrich) solution of a known concentration in three separate probes. 10 mL of KOI_3 solution was added to Erlenmeyer flask (250 mL), to which ~100 mg of KI (Bioultra > 99.5% TA from Sigma-Aldrich) and 2 mL of 6 M H_2SO_4 was added. The obtained I_3^- solution was immediately titrated with thiosulfate solution. Just before the endpoint, indicated by a light straw-like color, the starch solution was added resulting in a change of color to a dark red/brown (this color change is due to branched amylodextrin rather than blue when using straight chain amylose). The thiosulfate solution was prepared fresh the same day as the titration experiment. Titrations to determine $LiIO_3$ formed through reactions in I_3^- were performed by allowing the reaction to reach completion (indicated by the complete consumption of I_3^- based on the solution becoming colorless). The entirety of the solid and liquid phases were then transferred to an Erlenmeyer flask (rinsing the reaction vial three times with DI H_2O) and then titrated as per above.

Raman spectroscopy was performed on a LabRAM HR800 microscope (Horiba Jobin Yvon) using an external 20 mW He:Ne 633 nm laser (Horiba, Jobin Yvon), and focused with a 50× long working distance objective and a 10–0.3 neutral density filter. A silicon substrate was used to calibrate the Raman shift. An airtight cell was used for powders, and all samples were prepared in an argon-filled glovebox. Liquid samples were tightly sealed in a 2-mL vial and assessed using a 10× working length. Reference spectra of Li_2O_2, LiOH, LiOH-H_2O, and $LiIO_3$ are available in Figure S38. *In situ* Raman spectroscopy during the reaction between LiOH and I_3^- in DMSO (Figure S32) was obtained by focusing on the solution during the reaction between excess LiOH and I_3^- in a small 2-mL vial that was seal with parafilm.

XRD of discharged products and powders was performed on a Rigaku Smartlab diffractometer in Bragg–Brentano geometry. A domed airtight XRD cell holder from Panalytical was used to prevent exposing the electrodes to ambient atmosphere. Reference spectra for LiOH, LiOH-H_2O, Li_2O_2, LiI, $DMSO_2$, and $LiIO_3$ are available in Figure S41.

^{1}H NMR was performed on Bruker AVANCE and Bruker AVANCE III-400 MHz nuclear magnetic resonance (NMR) spectrometers. Samples were prepared by mixing 0.5 mL of the sample + 0.1 mL of DMSO-D6 (for NMR locking) + 10 μL of internal reference (either MeCN [Acetonitrile anhydrous, 99.8%, Sigma-Aldrich dried over molecular sieves] or 1,4-dioxane [anhydrous, 99.8%, Sigma-Aldrich, dried over molecular sieves] chosen to avoid overlap with peaks of interest).

Ionic conductivity was measured using Traceble 23226-505 conductivity meter. 0.5 M LiTFSI solutions in each solvent were prepared and measured in an argon-filled glovebox (MBraun, <0.1 ppm H_2O, <0.1% O_2) at 30°C.

Gas chromatography (GC) was performed using high purity argon (5.0, airgas) as a carrier gas flowing at ~12 sccm, through a glass cell. The cell was purged with Ar for 1 h, during the last 15 min of which, a background spectrum was taken. The reaction compartment contained 15 mL of DMSO with either Li_2O_2 formed from disproportionation or commercial LiOH suspended in solution with active stirring. In addition, 2 mL of I_3^- solution (0.2 M LiI + 50 mM I_2 in DMSO) was injected using a syringe that was sealed onto a port of the glass reaction cell prior to purging without exposure to ambient air. 1 mL of gas sample was injected into a gas chromatograph (GC, SRI 8610C in the Multi-Gas #3 configuration). Samples were injected after 2, 22, 42, and 62 min of reaction. GC was calibrated using 2,500 ppm O_2 + 17,000 ppm N_2 in argon gas mixture.

Li-O_2 Cell Assembly and Experiments

Li-O_2 cells consisted of a lithium metal negative electrode (Chemetall, Germany, 15 mm in diameter) and a carbon paper with gas diffusion layer positive electrode (FuelCellsEtc, F2GDL, LOT: TST008, 12.5 mm diameter). The carbon paper was dried for 24 h at 90°C under vacuum and transferred to a glove box ($H_2O < 0.1$ ppm, $O_2 < 0.1$ ppm, Mbraun, USA) without exposure to ambient air. Glass fiber (Whatman, GF-A/GF-F, 17 mm diameter) was dried at 150°C under vacuum overnight and was transferred to the glove box without exposure to ambient air. Li-ion conducting glass-ceramic electrolyte (19 mm diameter, 150 μm thick, LICGC, Ohara Corp) was dried at 80°C under vacuum overnight. Cells were constructed by placing a single piece of glass fiber separator on top of the lithium, adding 120 μL of liquid electrolyte, followed by the Li-ion conducting glass-ceramic electrolyte, another piece of glass fiber separator, another 120 μL of liquid electrolyte, and finally the carbon paper positive electrode. No 316 stainless steel current collector was used to avoid a reaction that was observed between the 316 stainless steel current collector and iodine formed during charge in some cells (see Figure S42). The origin of this corrosion is not fully understood and is worthy of further investigation as it poses challenges for the practical implementation of LiI as a redox mediator; however, adequate performance over a single charging cycle was acquired by simply avoiding the use of the current collector and restricting the electrolyte contact with the 316 stainless steel spring as much as possible. For cells not analyzed using DEMS, following assembly, cells were transferred to a connected second argon glove box (Mbraun, USA, $H_2O < 0.1$ ppm, $O_2 < 1\%$) without exposure to air and pressurized with dry O_2 (Airgas, 99.999% pure, $H_2O/CO/CO_2 < 0.5$ ppm) to 25 psi (gauge) to ensure that an adequate amount of O_2 was available. The oxygen pressure in the cell was measured using a pressure gauge during the experiments to confirm proper cell sealing. Electrochemical tests were conducted using a Biologic VMP3.

LiOH pre-loaded electrodes were prepared by drop casting a slurry (70% wt Vulcan Carbon, 20% wt anhydrous commercial LiOH, 10% wt PTFE) onto a neat carbon paper (Toray TGP-H-60, 12.5 mm diameter). The Vulcan carbon (VC), PTFE, and carbon paper were dried at 80°C under vacuum for 24 h and transferred to a glovebox (Mbraun, USA, $H_2O < 0.1$ ppm, $O_2 < 1\%$) without exposure to the ambient. In the glovebox, the LiOH and VC were ground into a homogenous mixture using a mortar and pestle and then added to a suspension of PTFE in DME. After allowing the mixture to stir for 1 h, the slurry was drop cast 50 μL at a time until the desired mass loading was achieved. Individual 12.5-mm pieces of carbon paper were weighed before and after drop casting to determine the amount of mixture deposited. Typical loadings of the VC/LiOH/PTFE mixture were 3.9–5.0 mg per electrode ($1.267\ cm^2$). Electrodes were additionally dried under vacuum for ~15 min to remove residual DME and were not exposed to ambient air during preparation.

Differential Electrochemical Mass Spectroscopy of Cells during Charging

A custom-made DEMS setup based on a design by McCloskey et al.,[80] which has been reported previously,[27,81,82] was used for assessing gas evolution during the charging process. O_2, CO, CO_2, H_2, and H_2O evolution during charge was quantified at 20-min intervals using a mass spectrometer coupled with pressure monitoring. Details of DEMS and cell technical construction are available online.[81] Argon (airgas, 99.999% pure, O_2, H_2O, $CO_2 < 1$ppm) was used as a carrier gas. In all cells, no detectable quantities of CO, H_2, and H_2O were detected, so these values are omitted from all figures. Cells were prepared as described above. Li-O_2 cells were first discharged under O_2 environment for 20 h at 0.05 mA/cm^2. The cell environment was then changed to argon by evacuating the cell and refilling it with argon five times and charged at 0.1 mA/cm^2 to a cutoff voltage of 4.5 V_{Li}. LiOH-pre-loaded electrodes were charged under argon environment at 0.1 mA/cm^2 to a cutoff voltage of 4.5 V_{Li}.

Mass spectroscopy on the gas headspace of a reaction vial was carried out by connecting a sealed vial to the DEMS setup described above. The reaction compartment contained 10 mL of DMSO with either Li_2O_2 formed from disproportionation or synthetic LiOH suspended in solution with active stirring. 1.5 mL of I_3^- solution (0.2 M LiI + 50 mM I_2 in DMSO) was injected using a syringe that was sealed onto a port of the reaction vial cell prior to purging without exposure to ambient air.

SUPPLEMENTAL INFORMATION

Supplemental Information includes Supplemental experimental procedures, 45 figures, and 3 tables and can be found with this article online at https://doi.org/10.1016/j.joule.2018.12.014.

ACKNOWLEDGMENTS

The work was supported in part by Toyota Motor Europe and the Skoltech Center for Electrochemical Energy Storage. SEM imaging, XRD measurements, and UV-vis spectroscopy were performed at the MRSEC Shared Experimental Facilities at MIT, supported by the National Science Foundation under award number DMR-1419807. G.L. was partially supported by a Natural Sciences and Engineering Research Council of Canada (NSERC) PGS-D. We would like to thank Jonathan Hwang for the assistance with GC measurements, Janet Nienhuis for experimental assistance, and Shuting Feng for helpful discussion.

AUTHOR CONTRIBUTIONS

Conceptualization, G.L., M.T., and Y.S.-H.; Methodology, G.L., M.T., and Y.S.-H.; Investigation, G.L., M.T., and R.T.; Writing – Original Draft, G.L. and Y.S.-H.; Writing – Review & Editing, G.L., M.T., R.T., F.B., and Y.S.-H.; Funding Acquisition, Y.S.-H.; Supervision, Y.S.-H.

DECLARATION OF INTERESTS

The authors declare no competing interests.

Received: September 1, 2018
Revised: October 31, 2018
Accepted: December 10, 2018
Published: January 17, 2019

REFERENCES

1. Aurbach, D., McCloskey, B.D., Nazar, L.F., and Bruce, P.G. (2016). Advances in understanding mechanisms underpinning lithium–air batteries. Nat. Energy *1*, 16128.
2. Bruce, P.G., Freunberger, S.A., Hardwick, L.J., and Tarascon, J.-M. (2012). Li–O2 and Li–S batteries with high energy storage. Nat. Mater *11*, 19–29.
3. Kwabi, D.G., Ortiz-Vitoriano, N., Freunberger, S.A., Chen, Y., Imanishi, N., Bruce, P.G., and Shao-Horn, Y. (2014). Materials challenges in rechargeable lithium-air batteries. MRS Bull. *39*, 443–452.
4. Lu, Y.-C., Gallant, B.M., Kwabi, D.G., Harding, J.R., Mitchell, R.R., Whittingham, M.S., and Shao-Horn, Y. (2013). Lithium–oxygen batteries: Bridging mechanistic understanding and battery performance. Energy Environ. Sci. *6*, 750.
5. Viswanathan, V., Nørskov, J.K., Speidel, A., Scheffler, R., Gowda, S., and Luntz, A.C. (2013). Li–O_2 kinetic overpotentials: tafel plots from experiment and first-principles theory. J. Phys. Chem. Lett. *4*, 556–560.
6. Kwabi, D.G., Bryantsev, V.S., Batcho, T.P., Itkis, D.M., Thompson, C.V., and Shao-Horn, Y. (2016). Experimental and computational analysis of the solvent-dependent O2/Li+-O2- redox couple: Standard potentials, coupling strength, and implications for lithium-oxygen batteries. Angew. Chem. Int. Ed. *55*, 1–7.
7. Johnson, L., Li, C., Liu, Z., Chen, Y., Freunberger, S.A., Ashok, P.C., Praveen, B.B., Dholakia, K., Tarascon, J.-M., and Bruce, P.G. (2014). The role of LiO2 solubility in O2 reduction in aprotic solvents and its consequences for Li–O2 batteries. Nat. Chem. *6*, 1091–1099.
8. Sharon, D., Hirsberg, D., Salama, M., Afri, M., Frimer, A.A., Noked, M., Kwak, W., Sun, Y.-K., and Aurbach, D. (2016). Mechanistic role of Li^+ dissociation level in aprotic Li–O2 Battery. ACS Appl. Mater. Interfaces *8*, 5300–5307.
9. Burke, C.M., Pande, V., Khetan, A., Viswanathan, V., and McCloskey, B.D. (2015). Enhancing electrochemical intermediate solvation through electrolyte anion selection to increase nonaqueous Li–O2 in battery capacity. Proc. Natl. Acad. Sci. USA *112*, 9293–9298.
10. Kwabi, D.G., Tułodziecki, M., Pour, N., Itkis, D.M., Thompson, C.V., and Shao-Horn, Y. (2016). Controlling solution-mediated reaction mechanisms of oxygen reduction using potential and solvent for aprotic lithium–oxygen batteries. J. Phys. Chem. Lett. *7*, 1204–1212.

11. Mitchell, R.R., Gallant, B.M., Shao-Horn, Y., and Thompson, C.V. (2013). Mechanisms of morphological evolution of Li$_2$O2 particles during electrochemical growth. J. Phys. Chem. Lett. *4*, 1060–1064.

12. McCloskey, B.D., Valery, A., Luntz, A.C., Gowda, S.R., Wallraff, G.M., Garcia, J.M., Mori, T., and Krupp, L.E. (2013). Combining accurate O$_2$ and Li$_2$O$_2$ assays to separate discharge and charge stability limitations in nonaqueous Li–O$_2$ batteries. J. Phys. Chem. Lett. *4*, 2989–2993.

13. Lim, H.-D., Lee, B., Zheng, Y., Hong, J., Kim, J., Gwon, H., Ko, Y., Lee, M., Cho, K., and Kang, K. (2016). Rational design of redox mediators for advanced Li–O2 batteries. Nat. Energy *1*, 16066.

14. Lim, H.-D., Song, H., Kim, J., Gwon, H., Bae, Y., Park, K.-Y., Hong, J., Kim, H., Kim, T., Kim, Y.H., et al. (2014). Superior rechargeability and efficiency of lithium-oxygen batteries: Hierarchical air electrode architecture combined with a soluble catalyst. Angew. Chem. Int. Ed. *53*, 3926–3931.

15. Liu, T., Leskes, M., Yu, W., Moore, A.J., Zhou, L., Bayley, P.M., Kim, G., and Grey, C.P. (2015). Cycling Li-O2 batteries via LiOH formation and decomposition. Science *350*, 530–533.

16. Bergner, B.J., Schürmann, A., Peppler, K., Garsuch, A., and Janek, J. (2014). TEMPO: a mobile catalyst for rechargeable Li-O$_2$ batteries. J. Am. Chem. Soc. *136*, 15054–15064.

17. Kwak, W.-J., Hirshberg, D., Sharon, D., Afri, M., Frimer, A.A., Jung, H.-G., Aurbach, D., and Sun, Y.-K. (2016). Li–O$_2$ cells with LiBr as an electrolyte and a redox mediator. Energy Environ. Sci. *9*, 2334–2345.

18. Kwak, W.-J., Hirshberg, D., Sharon, D., Shin, H.-J., Afri, M., Park, J.-B., Garsuch, A., Chesneau, F.F., Frimer, A.A., Aurbach, D., et al. (2015). Understanding the behavior of Li–oxygen cells containing LiI. J. Mater. Chem. A *3*, 8855–8864.

19. Chen, Y., Freunberger, S.A., Peng, Z., Fontaine, O., and Bruce, P.G. (2013). Charging a Li–O2 battery using a redox mediator. Nat. Chem. *5*, 489–494.

20. Sun, D., Shen, Y., Zhang, W., Yu, L., Yi, Z., Yin, W., Wang, D., Huang, Y., Wang, J., Wang, D., et al. (2014). A solution-phase bifunctional catalyst for lithium–oxygen batteries. J. Am. Chem. Soc. *136*, 8941–8946.

21. Feng, N., He, P., and Zhou, H. (2015). Enabling catalytic oxidation of Li2O2 at the liquid-solid interface: the evolution of an aprotic Li-O2 battery. ChemSusChem. *8*, 600–602.

22. Kundu, D., Black, R., Adams, B., and Nazar, L.F. (2015). A highly active low voltage redox mediator for enhanced rechargeability of lithium–oxygen batteries. ACS Cent. Sci. *1*, 510–515.

23. Torres, W.R., Herrera, S.E., Tesio, A.Y., del Pozo, M., and Calvo, E.J. (2015). Soluble TTF catalyst for the oxidation of cathode products in Li-oxygen battery: a chemical scavenger. Electrochim. Acta *182*, 1118–1123.

24. Wu, S., Tang, J., Li, F., Liu, X., and Zhou, H. (2015). Low charge overpotentials in lithium–oxygen batteries based on tetraglyme electrolytes with a limited amount of water. Chem. Commun. *51*, 16860–16863.

25. Zhu, Y.G., Jia, C., Yang, J., Pan, F., Huang, Q., and Wang, Q. (2015). Dual redox catalysts for oxygen reduction and evolution reactions: towards a redox flow Li–O$_2$ battery. Chem. Commun. *51*, 9451–9454.

26. Pande, V., and Viswanathan, V. (2017). Criteria and considerations for the selection of redox mediators in nonaqueous Li–O2 batteries. ACS Energy Lett. *2*, 60–63.

27. Yao, K.P.C., Frith, J.T., Sayed, S.Y., Bardé, F., Owen, J.R., Shao-Horn, Y., and Garcia-Araez, N. (2016). Utilization of cobalt bis(terpyridine) metal complex as soluble redox mediator in Li–O$_2$ batteries. J. Phys. Chem. C *120*, 16290–16297.

28. Zeng, X., Leng, L., Liu, F., Wang, G., Dong, Y., Du, L., Liu, L., and Liao, S. (2016). Enhanced Li-O 2 battery performance, using graphene-like nori-derived carbon as the cathode and adding LiI in the electrolyte as a promoter. Electrochim. Acta *200*, 231–238.

29. Zhang, W., Shen, Y., Sun, D., Huang, Z., Zhou, J., Yan, H., and Huang, Y. (2016). Promoting Li$_2$O$_2$ oxidation via solvent-assisted redox shuttle process for low overpotential Li-O 2 battery. Nano Energy *30*, 43–51.

30. Zhang, T., Liao, K., He, P., and Zhou, H. (2016). A self-defense redox mediator for efficient lithium–O$_2$ batteries. Energy Environ. Sci. *9*, 1024–1030.

31. Xu, J.-J., Xu, D., Wang, Z.-L., Wang, H.-G., Zhang, L.-L., and Zhang, X.-B. (2013). Synthesis of perovskite-based porous La$_{0.75}$Sr$_{0.25}$MnO$_3$ nanotubes as a highly efficient electrocatalyst for rechargeable lithium-oxygen batteries. Angew. Chem. Int. Ed. *52*, 3887–3890.

32. Yao, K.P.C., Risch, M., Sayed, S.Y., Lee, Y.-L., Harding, J.R., Grimaud, A., Pour, N., Xu, Z., Zhou, J., Mansour, A., et al. (2015). Solid-state activation of Li$_2$O$_2$ oxidation kinetics and implications for Li–O2 batteries. Energy Environ. Sci. *8*, 2417–2426.

33. Li, L., and Manthiram, A. (2014). O- and N-doped carbon nanowebs as metal-free catalysts for hybrid Li-air batteries. Adv. Energy Mater. *4*, 1301795.

34. Shui, J., Lin, Y., Connell, J.W., Xu, J., Fan, X., and Dai, L. (2016). Nitrogen-doped holey graphene for high-performance rechargeable Li–O$_2$ batteries. ACS Energy Lett. *1*, 260–265.

35. Yin, Y.-B., Xu, J.-J., Liu, Q.-C., and Zhang, X.-B. (2016). Macroporous interconnected hollow carbon nanofibers inspired by golden-toad eggs toward a binder-free, high-rate, and flexible electrode. Adv. Mater. *28*, 7494–7500.

36. Wong, R.A., Yang, C., Dutta, A., O, M., Hong, M., Thomas, M., Yamanaka, M.L., Ohta, T., Waki, K., and Byon, H.R. (2018). Critically examining the role of nanocatalysts in Li–O$_2$ batteries: viability toward suppression of recharge overpotential, rechargeability, and cyclability. ACS Energy Lett. *3*, 592–597.

37. Liang, Z., and Lu, Y.-C. (2016). Critical role of redox mediator in suppressing charging instabilities of lithium–oxygen batteries. J. Am. Chem. Soc. *138*, 7574–7583.

38. Xu, J.-J., Wang, Z.-L., Xu, D., Zhang, L.-L., and Zhang, X.-B. (2013). Tailoring deposition and morphology of discharge products towards high-rate and long-life lithium-oxygen batteries. Nat. Commun. *4*, 2438–2448.

39. Kwon, H.-M., Thomas, M.L., Tatara, R., Nakanishi, A., Dokko, K., and Watanabe, M. (2017). Effect of anion in glyme-based electrolyte for Li-O$_2$ batteries: stability/solubility of discharge intermediate. Chem. Lett. *41*, 573–576.

40. Radin, M.D., and Siegel, D.J. (2013). Charge transport in lithium peroxide: relevance for rechargeable metal–air batteries. Energy Environ. Sci. *6*, 2370.

41. Bergner, B.J., Hofmann, C., Schürmann, A., Schröder, D., Peppler, K., Schreiner, P.R., and Janek, J. (2015). Understanding the fundamentals of redox mediators in Li–O$_2$ batteries: a case study on nitroxides. Phys. Chem. Chem. Phys. *17*, 31769–31779.

42. Bergner, B.J., Busche, M.R., Pinedo, R., Berkes, B.B., Schröder, D., and Janek, J. (2016). How to improve capacity and cycling stability for next generation Li–O$_2$: Batteries: approach with a solid electrolyte and elevated redox mediator concentrations. ACS Appl. Mater. Interfaces *8*, 7756–7765.

43. Lee, D.J., Lee, H., Kim, Y.-J., Park, J.-K., and Kim, H.-T. (2016). Sustainable redox mediation for lithium-oxygen batteries by a composite protective layer on the lithium-metal anode. Adv. Mater. *28*, 857–863.

44. Burke, C.M., Black, R., Kochetkov, I.R., Giordani, V., Addison, D., Nazar, L.F., and McCloskey, B.D. (2016). Implications of 4 e^- oxygen reduction via iodide redox mediation in Li–O$_2$ batteries. ACS Energy Lett. *2*, 747–756.

45. Tułodziecki, M., Leverick, G.M., Amanchukwu, C.V., Katayama, Y., Kwabi, D.G., Bardé, F., Hammond, P.T., and Shao-Horn, Y. (2017). The role of iodide in the formation of lithium hydroxide in lithium–oxygen batteries. Energy Environ. Sci. *10*, 1828–1842.

46. Qiao, Y., Wu, S., Sun, Y., Guo, S., Yi, J., He, P., and Zhou, H. (2017). Unraveling the complex role of iodide additives in Li–O$_2$ batteries. ACS Energy Lett. *2*, 1869–1878.

47. Li, Y., Dong, S., Chen, B., Lu, C., Liu, K., Zhang, Z., Du, H., Wang, X., Chen, X., Zhou, X., et al. (2017). Li–O2 cell with LiI(3-hydroxypropionitrile)2 as a redox mediator: insight into the working mechanism of I^- during charge in anhydrous systems. J. Phys. Chem. Lett. *8*, 4218–4225.

48. Zhu, Y.G., Liu, Q., Rong, Y., Chen, H., Yang, J., Jia, C., Yu, L.J., Karton, A., Ren, Y., Xu, X., et al. (2017). Proton enhanced dynamic battery chemistry for aprotic lithium–oxygen batteries. Nat. Commun. *8*, 14308.

49. Kwabi, D.G., Batcho, T.P., Feng, S., Giordano, L., Thompson, C.V., and Shao-Horn, Y. (2016). The effect of water on discharge product growth and chemistry in Li–O$_2$ batteries. Phys. Chem. Chem. Phys. *18*, 24944–24953.

50. Torres, A.E., and Balbuena, P.B. (2018). Exploring the LiOH formation reaction mechanism in lithium–air batteries. Chem. Mater. *30*, 708–717.

51. Shen, Y., Zhang, W., Chou, S.-L., and Dou, S.-X. (2016). Comment on "Cycling Li-O_2 batteries via LiOH formation and decomposition". Science *352*, 667.

52. Viswanathan, V., Pande, V., Abraham, K.M., Luntz, A.C., McCloskey, B.D., and Addison, D. (2015). Cycling Li-O_2 batteries via LiOH formation and decomposition. Science *350*, 530–533.

53. Bentley, C.L., Bond, A.M., Hollenkamp, A.F., Mahon, P.J., and Zhang, J. (2015). Voltammetric determination of the iodide/iodine formal potential and triiodide stability constant in conventional and ionic liquid media. J. Phys. Chem. C *119*, 22392–22403.

54. Liu, T., Kim, G., Carretero-González, J., Castillo-Martínez, E., Bayley, P.M., Liu, Z., and Grey, C.P. (2016). Response to comment on "Cycling Li-O_2 batteries via LiOH formation and decomposition". Science *352*, 667.

55. Noviandri, I., Brown, K.N., Fleming, D.S., Gulyas, P.T., Lay, P.A., Masters, A.F., and Phillips, L. (1999). The decamethylferrocenium/decamethylferrocene redox couple: a superior redox standard to the ferrocenium/ferrocene redox couple for studying solvent effects on the thermodynamics of electron transfer. J. Phys. Chem. B *103*, 6713–6722.

56. Matsumoto, M., and Swaddle, T.W. (2004). The decamethylferrocene(+/0) electrode reaction in organic solvents at variable pressure and temperature. Inorg. Chem. *43*, 2724–2735.

57. Nakanishi, A., Thomas, M.L., Kwon, H.-M., Kobayashi, Y., Tatara, R., Ueno, K., Dokko, K., and Watanabe, M. (2018). Electrolyte composition in Li/O_2 batteries with LiI redox mediators: solvation effects on redox potentials and implications for redox shuttling. J. Phys. Chem. C *122*, 1522–1534.

58. Born, M. (1920). Volumen und hydratationswärme der Ionen. Z. Physik *1*, 45–48.

59. Atkins, P.W., and MacDermott, A.J. (1982). The Born equation and ionic solvation. J. Chem. Educ. *59*, 359.

60. Adamson, A.W., and Gast, A.P. (1997). Physical Chemistry of Surfaces, Sixth Edition.

61. Gallant, B.M., Kwabi, D.G., Mitchell, R.R., Zhou, J., Thompson, C.V., and Shao-Horn, Y. (2013). Influence of Li2O2 morphology on oxygen reduction and evolution kinetics in Li–O2 batteries. Energy Environ. Sci. *6*, 2518.

62. Yao, K.P.C., Kwabi, D.G., Quinlan, R.A., Mansour, A.N., Grimaud, A., Lee, Y.-L., Lu, Y.-C., and Shao-Horn, Y. (2013). Thermal stability of Li_2O_2 and Li_2O for Li-Air batteries: in situ, XRD and XPS studies. J. Electrochem. Soc. *160*, A824–A831.

63. Sharon, D., Afri, M., Noked, M., Garsuch, A., Frimer, A.A., and Aurbach, D. (2013). Oxidation of dimethyl sulfoxide solutions by electrochemical reduction of oxygen. J. Phys. Chem. Lett. *4*, 3115–3119.

64. Kwabi, D.G., Batcho, T.P., Amanchukwu, C.V., Ortiz-Vitoriano, N., Hammond, P., Thompson, C.V., and Shao-Horn, Y. (2014). Chemical instability of dimethyl sulfoxide in lithium–air batteries. J. Phys. Chem. Lett. *5*, 2850–2856.

65. Alei, M., Morgan, L.O., Wageman, W.E., and Whaley, T.W. (1980). The pH dependence of nitrogen-15 NMR shifts and coupling constants in aqueous imidazole and 1-methylimidazole. Comments on estimation of tautomeric equilibrium constants for aqueous histidine. J. Am. Chem. Soc. *102*, 2881–2887.

66. Schutte, L., Kluit, P.P., and Havinga, E. (1966). The substitution reaction of histidine and some other imidazole derivatives with iodine. Tetrahedron *22*, 295–306.

67. Gerritsen, C.M., Gazda, M., and Margerum, D.W. (1993). Non-metal redox kinetics: hypobromite and hypoiodite reactions with cyanide and the hydrolysis of cyanogen halides. Inorg. Chem. *32*, 5739–5748.

68. Lengyel, I., Epstein, I.R., and Kustin, K. (1993). Kinetics of iodine hydrolysis. Inorg. Chem. *32*, 5880–5882.

69. Xie, Y., McDonald, M.R., and Margerum, D.W. (1999). Mechanism of the reaction between iodate and iodide ions in acid solutions (Dushman reaction). Inorg. Chem. *38*, 3938–3940.

70. Wren, J.C., Paquette, J., Sunder, S., and Ford, B.L. (1986). Iodine chemistry in the +1 oxidation state. II. A Raman and uv–visible spectroscopic study of the disproportionation of hypoiodite in basic solutions. Can. J. Chem. *64*, 2284–2296.

71. Liu, T., Liu, Z., Kim, G., Frith, J.T., Garcia-Araez, N., and Grey, C.P. (2017). Understanding LiOH chemistry in a ruthenium-catalyzed Li-O_2 battery. Angew. Chem. Int. Ed. *56*, 16057–16062.

72. Cota, L.G., and de la Mora, P. (2005). On the structure of lithium peroxide, Li_2O_2. Acta Crystallogr. B *61*, 133–136.

73. Jones, L.H. (1954). The infrared spectra and structure of LiOH, LiOH•H2O and the deuterium species. Remark on fundamental frequency of OH -. J. Chem. Phys. *22*, 217–219.

74. Abrahams, S.C., and Kalnajs, J. (1955). The crystal structure of α-potassium superoxide. Acta Crystallogr. *8*, 503–506.

75. Farley, T.W.D., Hayes, W., Hull, S., Hutchings, M.T., and Vrtis, M. (1991). Investigation of thermally induced Li + ion disorder in Li 2 O using neutron diffraction. J. Phys. Condens. Matter *3*, 4761–4781.

76. Reid, C., and Mulliken, R.S. (1954). Molecular compounds and their spectra. IV. The pyridine-iodine System1. J. Am. Chem. Soc. *76*, 3869–3874.

77. Kolthoff, I.M., and Jordan, J. (1953). Voltammetry of iodine and iodide at rotated platinum wire electrodes. J. Am. Chem. Soc. *75*, 1571–1575.

78. Grassian, V.H., and Muetterties, E.L. (1986). Electron energy loss and thermal desorption spectroscopy of pyridine adsorbed on platinum(111). J. Phys. Chem. *90*, 5900–5907.

79. Black, R., Oh, S.H., Lee, J.-H., Yim, T., Adams, B., and Nazar, L.F. (2012). Screening for superoxide reactivity in Li-O batteries: effect on Li_2O_2/LiOH crystallization. J. Am. Chem. Soc. *134*, 2902–2905.

80. McCloskey, B.D., Bethune, D.S., Shelby, R.M., Girishkumar, G., and Luntz, A.C. (2011). Solvents' critical role in nonaqueous lithium–oxygen battery electrochemistry. J. Phys. Chem. Lett. *2*, 1161–1166.

81. Harding, J.R. (2015). Investigation of oxidation in nonaqueous lithium-air batteries. PhD thesis (Massachusetts Institute of Technology).

82. Harding, J.R., Amanchukwu, C.V., Hammond, P.T., and Shao-Horn, Y. (2015). Instability of poly(ethylene oxide) upon oxidation in lithium–air batteries. J. Phys. Chem. C *119*, 6947–6955.